

1 **RHEB/mTOR-hyperactivity causing cortical malformations drives seizures through**
2 **increased axonal connectivity**

3

4 Martina Proietti Onori^{1,2}, Linda M.C. Koene^{1,2,4}, Carmen B. Schafer^{1,4}, Mark Nellist³, Marcel de
5 Brito van Velze¹, Zhenyu Gao¹, Ype Elgersma^{1,2,*}, Geeske M. van Woerden^{1,2,*}

6 ¹Department of Neuroscience, Erasmus Medical Center, Rotterdam, Zuid Holland, 3015 GD, The Netherlands

7 ²The ENCORE Expertise Center for Neurodevelopmental Disorders, Erasmus Medical Center, Rotterdam, Zuid
8 Holland, 3015 GD, The Netherlands

9 ³Department of Clinical Genetics, Erasmus Medical Center, Rotterdam, Zuid Holland, 3015 GD, The Netherlands

10 ⁴These authors contributed equally

11 *Correspondence: y.elgersma@erasmusmc.nl (Y.E.), g.vanwoerden@erasmumc.nl (G.M.v.W.)

12

13 **ABSTRACT**

14 Dominant-active mutations in *Ras Homolog Enriched in Brain 1 (RHEB)*, such as the recently
15 identified RHEBp.P37L mutation, can cause malformations of cortical development (MCD) with
16 associated epilepsy and intellectual disability through a yet unknown mechanism. We found that
17 focal expression of RHEBp.P37L in mouse somatosensory cortex results in an MCD-like
18 phenotype, with increased mammalian target of rapamycin (mTOR) signaling, ectopic localization
19 of neurons and generalized seizures. In addition, the RHEBp.P37L expressing neurons showed
20 increased axonal length and branching. By temporally controlling RHEBp.P37L expression, we
21 found that the cortical malformation by itself was neither necessary nor sufficient to generate
22 seizures. Rather, seizures were contingent on persistent mTOR activation and enhanced axonal
23 connectivity of RHEBp.P37L expressing neurons, causing hyperexcitability of distally connected
24 neurons. These results provide new evidence of the extent of anatomical and physiological
25 abnormalities caused by mTOR hyperactivity, beyond local malformations, that can lead to
26 generalized epilepsy.

27

28 INTRODUCTION

29 Malformations of cortical development (MCD) are a heterogenous group of micro- and
30 macroscopic cortical abnormalities, such as focal cortical dysplasia (FCD), megalencephaly,
31 lissencephaly and periventricular nodular heterotopia (Barkovich et al., 2012). MCD arise from
32 disturbances in cortical development during early embryogenesis and are often linked to epilepsy
33 and intellectual disability (ID) (Juric-Sekhar and Hevner, 2019; Leventer et al., 2008; Represa,
34 2019). It is estimated that up to 40% of intractable or difficult to control childhood seizures are
35 due to MCD, and *vice versa*, at least 75% of the patients with MCD will develop seizures (Leventer
36 et al., 1999).

37 The mammalian (or mechanistic) target of rapamycin (mTOR) is a kinase that mediates
38 many cellular processes, including neuronal progenitors proliferation and cell growth (Laplante
39 and Sabatini, 2012; Saxton and Sabatini, 2017). mTOR forms 2 distinct protein complexes,
40 characterized by different binding partners, mTORC1 and mTORC2 (Bhaskar and Hay, 2007).
41 mTORC1 is regulated by the tuberous sclerosis complex (TSC) and the Ras Homolog Enriched in
42 Brain 1 (RHEB) (Parmar and Tamanoi, 2010). RHEB, a member of the RAS family of small
43 GTPases, is the direct activator of mTORC1 (Bai et al., 2007). The conversion of active GTP-
44 bound RHEB to the inactive GDP-bound form is mediated by the TSC complex, which acts as a
45 RHEB GTPase activating protein (GAP) (Li et al., 2004). In response to nutrients and growth
46 factors the TSC complex is inhibited, allowing activation of mTORC1 by RHEB-GTP (Manning
47 and Cantley, 2003; Sabatini, 2017). Studies in *Rheb* knock-out mice showed that RHEB activity
48 is the rate limiting step for mTOR activation in the brain, and that neuronal functioning in
49 particular is sensitive to increased RHEB-mTOR signaling (Goorden et al., 2015).

50 Hyperactivation of the mTOR pathway by mutations in genes encoding components of the
51 mTOR pathway (*e.g. AKT3, PIK3CA, DEPDC5, PTEN, TSC1, TSC2, RHEB* and *MTOR* itself) has
52 been associated with different types of MCD, such as megalencephaly and FCD, as well as with
53 epilepsy (Crino, 2011; Juric-Sekhar and Hevner, 2019; Moffat et al., 2015). The underlying genetic
54 variability explains the heterogeneity of MCD and illustrates the challenges involved in
55 understanding the mechanisms underlying MCD-associated epilepsy.

56 The discovery of genetic mutations that cause FCD or other types of MCD, allowed the
57 generation of animal models to study the development of MCD and associated epilepsy
58 (Chevassus-au-Louis et al., 1999; Wong and Roper, 2016). In particular, *in utero* electroporation
59 (IUE), that allows for the spatial and temporal control of transgene expression during embryonic
60 development, has been used to generate mouse models with focal malformations and epilepsy
61 (Hanai et al., 2017; Hsieh et al., 2016; Park et al., 2018; Ribierre et al., 2018).

62 One recent FCD mouse model was generated by using IUE to overexpress the
63 constitutively active RHEBp.S16H mutant (Yan et al., 2006). This results in mTOR hyperactivity,
64 FCD and spontaneous seizures (Hsieh et al., 2016). Recently we identified two *de novo* mutations
65 in *RHEB* (c.110C>T (p.P37L) and c.202T>C (p.S68P)) in patients with ID, epilepsy and
66 megalencephaly (Reijnders et al., 2017), providing for the first time a clinically relevant link
67 between RHEB and MCD. IUE of a construct encoding the RHEBp.P37L mutant caused severe
68 focal cortical lesions, resembling periventricular nodular heterotopia, and diffuse neuronal
69 misplacement in the cortex. Furthermore, the mice reliably developed spontaneous seizures
70 starting at three weeks of age (Reijnders et al., 2017). The anatomical and phenotypical features
71 of this novel mouse model, fully recapitulating the most prominent characteristics of MCD (focal

72 lesions and epilepsy), make this a powerful tool and clinically relevant novel model to study the
73 mechanisms underlying mTOR and MCD-related epilepsy.

74 Here we demonstrate that *RHEB* mutations that cause MCD in patients activate mTORC1
75 signaling and that the cortical malformation is not required for the development of mTOR related
76 seizures, in line with previous studies (Abs et al., 2013; Hsieh et al., 2016). Additionally, we
77 provide evidence that the presence of heterotopia by itself is insufficient to cause epilepsy. Instead,
78 we found that persistent activation of the mTOR pathway results in anatomical and functional
79 changes in axonal connectivity, which cause increased excitability of distally connected neurons
80 and the development of generalized seizures.

81

82 RESULTS

83 The RHEBp.P37L protein is resistant to TSC complex inhibition and causes aberrant 84 cortical development *in vivo*

85 The RHEBp.P37L mutation was identified in patients with ID, megalencephaly and epilepsy, and
86 it was proposed to act as a gain of function mutation (Reijnders et al., 2017). This could potentially
87 be due to resistance to the GAP-function of the TSC complex. To assess whether the TSC complex
88 can convert RHEBp.P37L from its active GTP- to its inactive GDP-bound state, we compared the
89 effects of transient *in vitro* overexpression of the RHEBp.P37L mutant with wild-type RHEB
90 (RHEB WT) and the RHEBp.S16H mutant, a well-known gain of function mutant of RHEB
91 recently used to generate an FCD mouse model (Hsieh et al., 2016; Yan et al., 2006). In the absence
92 of TSC, overexpression of RHEB WT as well as both RHEB mutants caused increased mTORC1
93 activity, as measured by T389-phosphorylation of co-expressed S6K, a direct substrate of the
94 mTORC1 kinase (**Figure 1A**, see **Supplementary table1** for statistics overview). In the presence
95 of the TSC complex, mTORC1 activity was reduced in the RHEB WT and RHEBp.S16H
96 expressing cells, but not in the RHEBp.P37L expressing cells (**Figure 1A**). Here, presence or
97 absence of TSC resulted in similar levels of S6K phosphorylation, confirming that the patient-
98 derived RHEBp.P37L acts as a gain of function mutation which is resistant to inhibitory action of
99 the TSC complex (**Figure 1A**).

100 Using IUE, we have previously shown that overexpression of the RHEBp.P37L mutant,
101 but not RHEB WT, results in the formation of a heterotopic nodule as well as spontaneous epilepsy
102 in 100% of the targeted mice (Reijnders et al., 2017), providing us with a valuable model to study
103 the mechanisms behind mTORC1-dependent and MCD-related epilepsy. To confirm previous
104 results and further characterize the model, we used IUE to introduce the RHEBp.P37L vector or

105 an empty vector control at E14.5 in progenitor cells that give rise to layer 2/3 (L2/3) pyramidal
106 neurons of the somatosensory cortex (SScx) (**Figure 1B**). As shown previously, overexpression of
107 RHEBp.P37L resulted in a clear migration deficit, with only 20% of the targeted cells reaching
108 the outer layers of the cortex (L2/3) compared to 97% in the empty vector condition (**Figure 1C**,
109 inset). The non-migrated transfected neurons remained in the white matter to form a heterotopic
110 nodule lining the ventricle in the adult brain (**Figure 1C** and **Figure 1-figure supplement 1**).

111 While the general cortical layer architecture remained intact (**Figure 1-figure supplement**
112 **1**, ectopic RHEBp.P37L overexpressing cells showed cytological abnormalities, with dysmorphic
113 appearance and enlarged soma size (**Figure 2A** and **Figure 1-figure supplement 1**). Sholl analysis
114 of biocytin filled cells in the heterotopic nodule of RHEBp.P37L expressing neurons revealed that
115 the cells in the nodule presented a more complex arborization compared to empty vector control
116 cells in L2/3 (**Figure 2B**). Transfected ectopic neurons preserved the molecular identity of mature
117 L2/3 pyramidal cells, being positive for the neuronal marker NeuN and the outer layer molecular
118 marker CUX1 and negative for the deeper layer marker CTIP2 (**Figure 2C** and **Figure 2-figure**
119 **supplement 1A**). Additionally, most neurons in the nodule were SATB2 positive, showing that,
120 despite being mislocalized, they maintained the callosal projection identity (**Figure 2C** and **Figure**
121 **2-figure supplement 1A**). Finally, mice overexpressing RHEBp.P37L showed an overall increase
122 in ribosomal protein S6 phosphorylation, a commonly used readout for mTORC1 activity, in the
123 transfected hemisphere compared to the empty vector condition (**Figure 2D** and **Figure 2-figure**
124 **supplement 1B**).

125 **Overexpression of RHEBp.P37L *in vivo* causes mTORC1-dependent spontaneous**
126 **generalized tonic-clonic seizures and abnormal neuronal network activity**

127 To assess the reliability of spontaneous seizures development, the RHEBp.P37L mice were
128 continuously monitored from weaning (P21) using wireless electroencephalography (EEG)
129 (**Figure 3A**). Spontaneous seizures started to appear at 3 weeks of age, with an average onset of
130 33 days, confirming previous data (Reijnders et al., 2017) (**Figure 3-figure supplement 1A**).
131 Seizures were highly stereotypical, characterized by the loss of upright posture followed by a tonic-
132 clonic phase with convulsions and twitching behavior. EEG recordings showed that, while control
133 mice did not show any epileptic activity (N = 6), all RHEBp.P37L mice (N = 12) showed clear
134 epileptic events (**Figure 3B** and **Figure 3-figure supplement 1B**). Seizures were characterized by
135 an increase in frequency and amplitude of brain activity (**Figure 3C**, box 3 ictal activity) compared
136 to baseline interictal activity (**Figure 3C**, box 2) and baseline activity of control mice (**Figure 3C**,
137 box 1). The calculated average duration of an epileptic event was 40 seconds (mean \pm SEM: 42.6
138 \pm 1.33), followed by a post-ictal depression phase of variable length (**Figure 3C**, box 4 post-ictal
139 activity). The frequency of seizures per day was variable between mice as well as per mouse over
140 time (**Figure 3-figure supplement 1C**). Additionally, no correlation was found between the total
141 number of seizures over three consecutive days of recording and the average number of targeted
142 cells per mouse (**Figure 3-figure supplement 1D**).

143 To assess if brain-wide suppression of mTORC1 activity could reduce seizures, we treated
144 a group of mice showing seizures (N=6; 5-6 weeks old) systemically for 7 days with the allosteric
145 mTORC1 inhibitor rapamycin (10 mg/kg). Rapamycin treatment reduced and temporarily
146 abolished the occurrence of seizures within one week from the last day of rapamycin
147 administration. However, seizures reoccurred starting 3 weeks after the last injection of rapamycin
148 in 4 out of 6 mice, indicating that sustained inhibition of mTORC1 is required to fully suppress
149 the seizures (data not shown).

150 Electrographic frequency dynamics of the interictal phases, and especially *theta*
151 oscillations, have been proven to be good predictors for epilepsy outcome, compared to
152 epileptiform spikes or high-frequency oscillations (HFOs), in several rodent models of epilepsy
153 (Chauvière et al., 2009; Milikovsky et al., 2017). Therefore, using local field potential (LFP)
154 recordings, we assessed the frequency dynamics of cortical brain activity in the interictal periods
155 of RHEBp.P37L expressing mice, starting from 4 weeks of age (**Figure 3D**). The normalized
156 averaged power spectrum of the RHEBp.P37L group did not reveal a significant difference
157 between the targeted and non-targeted cortex (targeting: $F(1, 22)=1.43$, $p=0.25$, non-significant,
158 Two-way repeated measure ANOVA; data not shown), therefore measurements from both sides
159 were pooled. Whereas the total power across 5 days of recording did not differ between the
160 RHEBp.P37L (N=12) and the control group (N=8) (Mann-Whitney $U = 157$, $p = 0.35$, non-
161 significant, two-tailed Mann-Whitney test, data not shown), a significant difference in the *delta*
162 (2-4 Hz), *theta* (4-8 Hz) and *gamma* (30-50 Hz) frequency bands of the normalized power
163 spectrum was seen in the RHEBp.P37L group compared to the control group (**Figure 3E, 3F** and
164 **Figure 3-figure supplement 1E and 1F**; statistics in **Supplementary table2**). The difference in
165 the *theta* and *gamma* frequency bands, but not in the *delta*, could be reverted to the control
166 condition by injecting the RHEB mice with 10 mg/kg rapamycin intraperitoneally for 3
167 consecutive days (**Figure 3E, 3F** and **Figure 3-figure supplement 1E and 1F**; statistics in
168 **Supplementary table2**). Together with the finding that rapamycin abolished seizures, this result
169 indicates that *theta* oscillations, which negatively correlate with *gamma* frequencies (Milikovsky
170 et al., 2017), are a good predictor for epileptogenesis in the RHEBp.P37L mouse model.

171

172

173 **The heterotopic nodule is neither necessary nor sufficient to induce spontaneous seizures**

174 Cortical malformations occur during early embryonic development and are generally associated
175 with the development of epileptic activity (Represa, 2019). Therefore, a transient treatment with
176 mTOR inhibitors during brain development might prevent the formation of a cortical malformation
177 and could consequently reduce the chances of developing epilepsy. To assess if early transient
178 down-regulation of the mTORC1 pathway upon overexpression of RHEBp.P37L could prevent
179 the development of heterotopic nodules, we injected pregnant female mice with 1 mg/kg of
180 rapamycin for 2 consecutive days starting 1 day after IUE of the RHEBp.P37L vector (**Figure**
181 **4A**). Prenatal down-regulation of the mTORC1 pathway significantly improved the migration of
182 the targeted neurons, with 75% of the targeted cells successfully migrating out (**Figure 4B**). In
183 addition, prenatal rapamycin treatment successfully prevented the formation of a heterotopic
184 nodule in 9 out of 11 mice. However, 7 out of the 11 targeted mice (58%) still showed spontaneous
185 seizures, including 5 mice that did not develop a discernable heterotopic nodule (**Figure 4C**).
186 Average onset of seizures was comparable to the non-treated RHEBp.P37L mice (mean \pm SEM:
187 32.6 days \pm 2.3; Chi square (1) = 0.16, p = 0.69, Log-rank test, data not shown). Hence, the
188 presence of a heterotopic nodule is not required for RHEBp.P37L mediated seizures, and reducing
189 the formation of these nodules does not always prevent epileptogenesis.

190 When comparing the cortical migration patterns in mice with and without seizures, a
191 clear correlation was observed between the migration pattern of RHEBp.P37L expressing cells
192 and the presence or absence of seizures: RHEBp.P37L-prenatal treated mice with seizures showed
193 a more severe migration deficit of RHEBp.P37L expressing cells compared to prenatal treated
194 RHEBp.P37L expressing mice that were seizure free (**Figure 4D**). In fact, the percentage of cells
195 that reached L2/3 of the SSex of RHEBp.P37L-prenatal treated mice with seizures (63%), was

196 significantly lower than RHEBp.P37L-prenatal treated mice without seizures (93%) or control
197 mice (98%) (% targeted cells in L2/3: $H(2) = 22.08, p < 0.0001$, Kruskal-Wallis test; empty vector
198 vs RHEBp.P37L-no seizures, $p > 0.99$; empty vector vs RHEBp.P37L-seizures, $p < 0.0001$;
199 RHEBp.P37L-no seizures vs RHEBp.P37L-seizures, $p = 0.002$; Dunn's multiple comparisons test,
200 data not shown). These results indicate that ectopic cells do facilitate the process of
201 epileptogenesis.

202 Hyperactivation of mTORC1 is sufficient to cause seizures, independent of the presence
203 of cortical malformations (Abs et al., 2013), even when the mTORC1 activity is increased in a
204 limited set of neurons (Hsieh et al., 2016). Moreover, the cortical malformation by itself, in the
205 absence of continued mTORC1 signaling, does not cause epilepsy, as was also shown by brain-
206 wide inhibition of mTORC1 signaling (Hsieh et al., 2016). To further dissect the relationship
207 between increased mTOR activity, cortical malformations and epilepsy, we made use of a genetic
208 approach, that allowed us not only to regulate mTORC1 activity in a temporal fashion, but also to
209 restrict its activity to a limited number of cells. To that end we used IUE to introduce a Lox-Stop-
210 Lox(LSL)-RHEBp.P37L vector or floxed-RHEBp.P37L vector together with a vector expressing
211 the ERT2CreERT2 fusion protein (**Figure 4E**). This allowed us to switch the RHEBp.P37L gene
212 respectively on or off during different stages of cortical development by means of systemic
213 tamoxifen administration. The use of an additional vector that expresses EGFP in a Cre-dependent
214 manner (CAG-DIO-EGFP), allowed us to assess the efficiency of Cre activation upon tamoxifen
215 administration. IUE of the LSL-RHEBp.P37L construct in the absence of tamoxifen
216 administration, did not result in a migration deficit, or seizures. This indicates that the LSL cassette
217 successfully prevented RHEBp.P37L expression (**Figure 4F**). However, once expression of
218 RHEBp.P37L was induced by administration of tamoxifen either at P7 or P21, a subset of the

219 mutant mice (38% of the P7 group and 50% of the P21 group) developed spontaneous seizures
220 (**Figure 4G**), albeit with a delayed onset compared to mice that express RHEBp.P37L throughout
221 development (Chi square (2) = 10.18, $p = 0.006$; Log-rank test, data not shown). This indicates that
222 RHEBp.P37L expression in a limited number of cells, can drive seizures in the absence of an
223 observable cortical malformation (migration defects or heterotopic nodules).

224 To investigate if presence of the heterotopic nodule is epileptogenic after normalizing
225 mTORC1 activation only in the targeted cells (instead of brain-wide as others also did in previous
226 studies (Hsieh et al., 2016)), we used IUE to insert the floxed-RHEBp.P37L vector (**Figure 4H**).
227 Upon expression of RHEBp.P37L during early pre- and postnatal development, we normalized
228 mTORC1 activity in these cells by inducing RHEBp.P37L deletion at P14. (**Figure 4I**). Although
229 a clear heterotopic nodule was formed in these mice, none of the mice developed seizures (**Figure**
230 **4I**). Furthermore, inducing deletion of RHEBp.P37L after epileptogenesis, completely abolished
231 the seizures within 10 days from gene deletion (N=4, last EEG measurements performed between
232 day 85 and 90) (**Figure 4I**). Taken together, these results indicate that cortical malformations are
233 neither necessary nor sufficient for the development of spontaneous seizures in our mouse model.

234

235 **RHEBp.P37L expression induces aberrant axonal development both *in vitro* and *in vivo* and** 236 **functional increased contralateral L2/3 and L5 connections**

237 The mTOR pathway plays an important role in axonal outgrowth, with functional effects on
238 neuronal network formation (Choi et al., 2008; Gong et al., 2015; Nie et al., 2010). Because
239 increasing mTOR signaling in a limited number of neurons in the brain is enough to cause seizures,
240 independently from cell misplacement, we hypothesized that this could be due to aberrant neuronal
241 connectivity caused by RHEBp.P37L overexpression. Therefore, we investigated the effect of

242 RHEBp.P37L on axonal length and branching. Overexpression of RHEBp.P37L in primary
243 hippocampal neurons *in vitro* caused a significant increase in axonal length and axonal branching,
244 compared to the empty vector control (**Figure 5A**).

245 *In vivo*, axons from callosal projection neurons originating from the superficial layers
246 of the SS_{Cx} project to the homotopic contralateral hemisphere, where they mostly innervate L2/3
247 and L5 pyramidal neurons (Fenlon et al., 2017; Petreanu et al., 2007). They also send collaterals
248 to L2/3 and, more strongly, L5 pyramidal neurons within the same column ipsilaterally,
249 participating in local circuitry (Fame et al., 2011; Petreanu et al., 2007). Therefore, it is conceivable
250 that *in vivo* overexpression of RHEBp.P37L affects callosal projections to the non-targeted
251 contralateral hemisphere. Analysis of the contralateral callosal axonal growth in matched coronal
252 sections with comparable targeting revealed that upon RHEBp.P37L overexpression, axonal
253 terminals in the contralateral hemisphere, show a broader distribution compared to controls,
254 reaching the primary (S1) and secondary (S2) SS_{Cx} (**Figure 5B**). Furthermore, a significant
255 difference was found in the distribution of the axonal terminals across the different layers in the
256 contralateral hemisphere. While in the control condition most of the terminals were located in
257 L2/3, with a lower abundance in L5 (Fenlon et al., 2017), in the RHEBp.P37L mice we found that
258 most of the terminals were located in the deeper layers of the cortex, suggesting an improper
259 cortical connectivity (**Figure 5C**). Furthermore, zooming in on the axonal projections on the
260 contralateral cortex revealed the presence of enlarged *boutons* and terminals in the RHEBp.P37L
261 mice that were both Synapsin-1 and VGLUT1 positive, markers for synaptic vesicles and
262 glutamatergic neurons, respectively (**Figure 5-figure supplement 1**).

263 To investigate if the contralateral axonal projections with these synaptic terminals showing
264 altered morphology are functional, we made use of optogenetics. We used IUE to introduce

265 channelrhodopsin-2 (pCAGGS-ChR2-Venus) (Petreanu et al., 2007) together with either the
266 empty vector control or the RHEBp.P37L construct in targeted neurons and recorded the
267 postsynaptic responses (EPSCs) to widefield optogenetic stimulation by patch-clamping L2/3 and
268 L5 pyramidal neurons in the (non-targeted) contralateral S1 where axonal terminals could be
269 observed (**Figure 6A and Figure 6-figure supplement 1A**). Analyzing the amplitude of EPSCs
270 following optogenetic stimulation in L5 and L2/3 of the contralateral S1, we observed an overall
271 increase in response in the RHEBp.P37L condition compared to the empty vector control condition
272 (see **Supplementary table 3** for statistics) (**Figure 6B**). When analyzing the total charge of the
273 compound postsynaptic response we observed similar response patterns (**Supplementary table 3**
274 for statistics) (**Figure 6B**). Bath application of tetrodotoxin (TTX) in the RHEBp.P37L group
275 decreased the post-synaptic responses evoked by photo-stimulating ChR2 expressing fibers to
276 noise level, which is indicative of action potential driven neurotransmitter release (**Figure 6-figure**
277 **supplement 1B**). The basic properties (resting membrane potential [V_m] and membrane resistance
278 [R_m]) of L2/3 and L5 contralateral cells in empty vector control and RHEBp.P37L conditions
279 were not different (**Supplementary table 3** for statistics). These data suggest increased synaptic
280 connectivity to the contralateral S1 upon overexpression of RHEBp.P37L.

281

282 **Loss of axonal projections or blocking vesicle release of RHEBp.P37L expressing neurons is** 283 **sufficient to stop seizures**

284 Having shown that the RHEBp.P37L expressing neurons show stronger axonal innervation and
285 synaptic connectivity to neurons in the contralateral hemisphere, we investigated whether these
286 altered neuronal projections drive the seizures. To assess this, we made use of the Tetanus toxin
287 light chain, known to specifically cleave the SNARE-complex protein Synaptobrevin/VAMP2

288 (Syb2) (Schiavo et al., 1992). VAMP2 is part of the SNARE complex that allows synaptic vesicles
289 fusion and the release of neurotransmitters (Gaisano et al., 1994) and recently it has been shown
290 to mediate the vesicular release of Brain Derived Neurotrophic Factor (BDNF) from axon and
291 dendrites, thereby regulating proper cortical connectivity (Shimojo et al., 2015). Intrinsic neuronal
292 activity during early brain development is crucial for axonal growth and branching, and blocking
293 synaptic transmission using Tetanus toxin interferes with proper cortical axonal formation,
294 resulting in the reduction and disappearance of axonal projections (Wang et al., 2007). Indeed,
295 when RHEBp.P37L was co-transfected with a Tetanus toxin construct (TeTxLC) that is active
296 during embryonic development, we observed a complete block of callosal axonal growth (**Figure**
297 **7A, 7B**). Furthermore, the mice targeted with the RHEBp.P37L and TeTxLC constructs did not
298 develop any seizures, suggesting that the abnormal axonal connectivity might mediate the
299 expression of seizures in our mouse model (**Figure 7B**).

300 The complete loss of callosal axonal branching upon embryonic activation of TeTxLC,
301 prevented us from testing whether increased synaptic transmission drives seizure development.
302 Therefore, to enable activation of the Tetanus toxin upon Tamoxifen injection at post-
303 developmental stages, we generated an inducible LSL-TeTxLC construct (**Figure 7C**) and co-
304 transfected this construct with RHEBp.P37L and the CAGG-ERT2CreERT2 vector (see **Figure**
305 **4E**). This allowed us to assess whether, once (abnormal) axonal projections are established,
306 blocking vesicular release either prevents the development of seizures, or stops seizures once they
307 have developed. Activation of the Tetanus toxin during postnatal development, but before seizure
308 onset (P14), completely prevented the development of seizures while allowing the axons to grow
309 and branch to the contralateral side (**Figure 7D**). Administering tamoxifen in 5 weeks old mice,
310 when the cortical connectivity is complete and after the mice showed seizures revealed that

311 epilepsy is not an irreversible process (**Figure 7D**). Already after 2 days of tamoxifen
312 administration, 3 out of 6 mice (**Supplementary table 4**) stopped showing any seizures and 2
313 weeks after the last tamoxifen injection all mice appeared to be seizure free (**Supplementary table**
314 **4**). These results indicate that inhibiting synaptic transmission by blocking vesicular release from
315 the targeted cells is enough to stop the occurrence of seizures in our mouse model.

316

317 **Neurons in the contralateral homotopic cortical area in RHEBp.P37L expressing mice show** 318 **increased excitability**

319 To obtain more insight into the cellular mechanisms that underlie epilepsy in our model, we used
320 whole-cell patch clamp to measure intrinsic physiological properties of the RHEBp.P37L
321 expressing neurons, of (ipsilateral) neurons directly surrounding the targeted cells, and of the
322 contralateral neurons in homotopic cortical areas (**Figure 8A**). Whole cell patch clamp recordings
323 were performed by recording from pyramidal neurons in S1 of 3 weeks old mice. For the
324 RHEBp.P37L expressing neurons (tdTomato positive), we recorded only from neurons that
325 managed to migrate out to L2/3 of S1 to be able to compare their physiological properties with
326 ‘empty vector’ control cells in L2/3 that expressed the tdTomato gene without expressing the
327 RHEBp.P37L protein (**Figure 8A**). RHEBp.P37L expressing neurons showed an increase in the
328 capacitance (C_m) compared to empty vector control cells (**Figure 8B** and see **Supplementary**
329 **table 5** for statistics), which is consistent with the increase in soma size (median of control empty
330 vector cells L2/3: 1.005, n cells=22; median RHEBp.P37L cells L2/3: 1.377, n cells=24; Mann-
331 Whitney U = 105, $p=0.0003$, Two-tailed Mann-Whitney test, data not shown). Additionally, the
332 membrane resistance (R_m) was decreased, whereas the resting membrane potential (V_m) was
333 unchanged compared to empty vector control cells (**Figure 8B** and see **Supplementary table 5**

334 for statistics). Depolarizing the neurons with increasing current injections, showed that the
335 excitability of cells expressing the empty vector were not different from non-targeted neurons in
336 the same mice or compared to non-targeted mice (**Figure 8-figure supplement 1**). In contrast,
337 RHEBp.P37L expressing neurons were hypoexcitable compared to control neurons measured in
338 mice expressing the empty vector as well as to non-targeted neurons ipsilateral and contralateral
339 (**Figure 8C** and see **Supplementary table 5** for statistics), without a change in the threshold V_m
340 to fire action potentials ($F(3, 94) = 0.59, p=0.62$, non-significant, One-way ANOVA). This result
341 is again in agreement with the observed increased soma size and concomitant increased cell
342 capacitance and decreased membrane resistance. Notably, while ipsilateral non-transfected
343 neurons surrounding the RHEBp.P37L expressing neurons in mice did not show changes in
344 excitability compared to empty vector control, non-transfected neurons in L2/3 on the contralateral
345 hemisphere showed a significant increase in excitability (**Figure 8C** and see **Supplementary table**
346 **5** for statistics), suggesting that the ectopic cells affect long-range connected neurons.

347 To experimentally address if the aberrant connectivity could cause the increase in
348 excitability in neurons on the contralateral cortex, we again made use of the inducible LSL-
349 TeTxLC construct and co-transfected this construct with RHEBp.P37L and the CAGG-
350 ERT2CreERT2 vector to enable activation of the Tetanus toxin upon Tamoxifen injection at post-
351 developmental stages (See **Figure 7C**). Whole-cell patch clamp recordings revealed that activating
352 the Tetanus toxin early during development (P14) (**Figure 8D**), completely reversed the
353 hyperexcitability phenotype of the contralateral non-targeted cells observed in the RHEBp.P37L
354 mice (**Figure 8E**) while the targeted cells co-transfected with the RHEBp.P37L and the Tetanus
355 toxin maintained the hypoexcitable phenotype and the basic properties observed in the
356 RHEBp.P37L group (**Figure 8E-F** and see **Supplementary table 6** for statistics). Taken together,

357 these data indicate that the abnormal axonal connectivity caused by RHEBp.P37L overexpression
358 is the primary driver of the hyperexcitability phenotype of contralateral L2/3 pyramidal neurons,
359 which in turn could be the main driver of epilepsy.

360 **DISCUSSION**

361 In this study, we investigated the mechanisms behind the spontaneous tonic-clonic seizures in a
362 mouse model that was generated by spatially and temporally restricted overexpression of a mTOR-
363 related ID mutation in *RHEB* (Reijnders et al., 2017). We showed that the RHEBp.P37L mutant is
364 resistant to inhibition by the TSC complex, and that restricted overexpression causes mTORC1
365 hyperactivity and the development of heterotopia with typical cellular features of human MCD
366 such as enlarged dysplastic neurons with altered morphology and mTORC1 activation.
367 Furthermore, the presence of cortical malformations is accompanied by the development of
368 spontaneous tonic-clonic seizures and alterations of the cortical brain dynamics that are rescued
369 by administration of rapamycin, an mTOR inhibitor. Using a pharmacological and genetic
370 approach we showed that the presence of the cortical malformation by itself is neither necessary
371 nor sufficient to induce epilepsy, while blocking either mTOR activity or vesicle release from these
372 cells is enough to stop or prevent seizures.

373 Similar to previously generated IUE mouse models of MCD, our model developed clear
374 heterotopia, strikingly resembling focal human cortical malformations, associated with mTORC1
375 hyperactivity and reliable spontaneous seizures (Hanai et al., 2017; Hsieh et al., 2016; Lim et al.,
376 2015; Park et al., 2018; Ribierre et al., 2018). The malformation in our mouse model is
377 characterized by white matter heterotopia and neuronal misplacement across the different cortical
378 layers, but maintains the molecular fingerprint belonging to L2/3 neurons. However, it is difficult
379 to categorize it as a specific type of MCD because it expresses characteristics of both FCD type I
380 and type IIa (with no Balloon cells observed) (Barkovich et al., 2012). Nonetheless, the targeted
381 cells have features common to several types of mTOR dependent MCD, including enlarged and
382 dysplastic cells with mTORC1 hyperactivation (Crino, 2011).

383 Previously it has been shown that brain wide activation of the mTOR pathway is
384 sufficient to induce seizures in the absence of any cortical malformations (Abs et al., 2013).
385 However, these models do not address the role of mTOR signaling in MCD related
386 pathophysiology. To address that, an elegant IUE mouse model was generated which expressed
387 the constitutive active RHEBp.S16H protein. These mice showed a migration deficit resembling
388 FCD and spontaneous epilepsy (Hsieh et al., 2016). Using this mouse model, it was also shown
389 that the presence of a cortical malformation is not necessary to induce seizures (Hsieh et al., 2016).
390 Notably, these mice did not show epilepsy when the SScx was targeted, and hence the investigators
391 suggested that the SScx might be a non-epileptogenic area. This is in contrast with our mouse
392 model using the human ID-related RHEBp.P37L mutant, where targeting the S1 area of the SScx,
393 reliably induces seizures. One reason for these contradictory findings might be the effect of the
394 mutation on RHEB function, as we showed that the RHEBp.S16H mutant could be partially
395 inhibited by the TSC complex, whereas the RHEBp.P37L mutant was insensitive to TSC
396 regulation.

397 Our mouse model offers a good tool to test novel AEDs *in vivo*. However, considering
398 the variability in the number of seizures exhibited, it will be beneficial to focus on different
399 parameters when assessing the potential therapeutic efficiency of AEDs. For this purpose, the *theta*
400 frequency oscillation, which we found to be affected and normalized upon rapamycin treatment,
401 represents a good biomarker for assessing the potential therapeutic value of treatments in our
402 mouse model (Chauvière et al., 2009; Milikovsky et al., 2017).

403 Everolimus and rapamycin (Sirolimus) have been shown in randomized controlled trials
404 to be beneficial for treating TSC associated epilepsy (Iris E Overwater et al., 2019; Overwater et
405 al., 2016), but not for treating the cognitive deficits (Krueger et al., 2017; Iris E. Overwater et al.,

406 2019). In this study we investigated the potential of a short prenatal rapamycin treatment in
407 improving both malformation defects and epilepsy, but preventing the possible side effects
408 (developmental delays and poor gain weight) (Tsai et al., 2013). We showed that a 2-day
409 rapamycin treatment during a critical time point of prenatal development can cause a substantial
410 improvement of the cortical malformation defects and prevent the development of seizures in
411 almost 50% of the cases. Future studies will have to assess if a combination of prenatal and
412 postnatal treatment with rapamycin in mice can be sufficient to significantly reduce the epileptic
413 events, as shown for brain malformations, without causing major side effects (Tsai et al., 2013;
414 Way et al., 2012).

415 Surgery is often an alternative to AEDs for treating MCD-related epilepsy. Human
416 electrophysiological findings show that seizures can often have multiple starting points, besides
417 the brain lesion itself (Chassoux et al., 2008; Major et al., 2009). Therefore, from a clinical point
418 of view, it is important to determine whether seizures originate from cells surrounding the cortical
419 malformation. Even though EEG and LFP do not have the spatial resolution to assess the primary
420 epileptogenic zone in our model, we showed that persistent mTORC1 hyperactivation in the
421 targeted cells is the primary cause of epilepsy. In fact, genetically removing the RHEBp.P37L
422 mutant, either before or after seizure development, was sufficient to prevent or stop the epilepsy.

423 Surprisingly, when exploring the causes of epileptogenesis, we observed that the
424 neurons expressing the RHEBp.P37L are hypoexcitable, which is consistent with the increase in
425 soma size but does not provide an obvious physiological explanation for the seizures observed in
426 our mouse model. However, we observed a clear increase of intrinsic excitability and in
427 postsynaptic responses upon optogenetic stimulation of RHEBp.P37L cells in contralateral
428 homotopic S1 cells. This suggests that RHEBp.P37L expressing cells induce cellular changes in

429 anatomically connected neurons, which might underlie, or at least exacerbate, the epilepsy
430 phenotype. Notably, these alterations extend well beyond the cells surrounding the cortical
431 malformation, as we found physiological changes were present contralateral to the targeted side.
432 Considering the abnormal axonal connectivity seen in our mouse model, this raises the possibility
433 that other anatomically connected cortical and sub-cortical areas not analyzed in this study might
434 also be affected, thereby providing an explanation for how a small percentage of targeted
435 hypoexcitable cells, independent of their location, can lead to generalized epilepsy. Therefore we
436 propose a model in which subtle microscopic alterations and aberrant connectivity, either through
437 an increase in synaptic connections or an increase in the strength of synaptic contacts caused by
438 mTOR hyperactivity, are sufficient to drive epileptogenesis.

439 By increasing axonal connectivity, RHEBp.P37L expressing neurons could potentially
440 alter synaptically connected neurons through neurotransmitter release. But they can also affect
441 neighboring (including synaptically non-connected) cells through the release of extracellular
442 vesicles such as exosomes (Budnik et al., 2016). The vesicles might mediate pathogenicity as was
443 previously shown *in vitro* (Patel et al., 2015). With the use of Tetanus toxin, we showed that the
444 effects on the contralateral side are directly driven by the abnormal enhanced axonal connectivity,
445 since blocking vesicle release specifically from the RHEBp.P37L expressing neurons, completely
446 rescued the epilepsy and normalized the intrinsic firing properties of the non-targeted contralateral
447 neurons. Tetanus toxin is primarily used to block synaptic transmission due to its effect on
448 neurotransmitter release, acting on the SNARE complex protein VAMP2 (Schiavo et al., 1992).
449 Given the observed increased axonal connectivity and the finding that distally connected cells were
450 physiologically affected, this strongly suggest that neurotransmitter mediated communication is
451 primarily causing the epilepsy phenotype. This notion is further supported by the optogenetics

452 experiments that showed increase postsynaptic responses upon stimulating the RHEBp.P37L
453 expressing neurons. While it has been proposed that specific tetanus insensitive VAMP proteins
454 (such as VAMP7) are involved in the release of exosomes into the extracellular space (Fader et
455 al., 2009), we cannot exclude the additional contribution of other types of vesicles to the observed
456 phenotype. Recently it was shown that Tetanus toxin sensitive SNAREs also drive the release of
457 BDNF (Shimojo et al., 2015). Some studies suggest that BDNF might contribute to epileptogenesis
458 (Binder et al., 2001), suggesting that abnormal BDNF signaling could further increase the epileptic
459 phenotype seen in our mouse model. Understanding the contribution of these different signaling
460 pathways is important for the development of targeted therapeutic strategies to treat MCD
461 associated epilepsy.

462 In summary, in this study we show that restricted overexpression of a hyperactive RHEB
463 mutant that was previously identified in patients with ID, megalencephaly and epilepsy, strongly
464 mimics the human MCD-like phenotype with mTOR pathway hyperactivity and seizures. We
465 provided pharmacological and genetic evidence that the cortical malformation *per se* is neither
466 necessary nor sufficient to induce seizures. Furthermore, we show that only a few neurons with
467 increased mTOR activity can be the driving force behind MCD-related epilepsy through aberrant
468 connectivity, resulting in increased excitability of distant non-targeted neurons, which can be
469 reversed by blocking vesicular release.

470 MATERIALS AND METHODS

471 Mice

472 Unless subjected to a surgical procedure, all experimental mice were kept group-housed in IVC
473 cages (Sealsafe 1145T, Tecniplast) with bedding material (Lignocel BK 8/15 from Rettenmayer)
474 on a 12/12 hr light/dark cycle at 21°C ($\pm 1^\circ\text{C}$), humidity at 40-70% and with food pellets
475 (801727CRM(P) from Special Dietary Service) and water available *ad libitum*. For the neuronal
476 cultures, FvB/NHsD females were crossed with FvB/NHsD males (both ordered at 8-10 weeks old
477 from Envigo). For the IUE, females FvB/NHsD (Envigo) were crossed with males C57Bl6/J
478 (ordered at 8-10 weeks old from Charles River). Both females and males from the *in utero*
479 electroporation litters were included in the experiments and no prescreening for successful
480 electroporation was performed before recruitment in the studies. Young (starting from P7) and
481 adult mice were used and the specific age for each experiment is indicated either in the results
482 section or in the figures' legends. Activation of the ERT2CreERT2 fusion protein (Matsuda and
483 Cepko, 2007) was achieved by intraperitoneal administration of tamoxifen for 4 consecutive days
484 (0.1 mg/g of bodyweight) dissolved in sunflower oil (20 mg/ml) at the ages specified in the results
485 section and in the figures. For inhibition of the mTOR pathway, rapamycin (Sigma-Aldrich) was
486 dissolved in dimethylsulfoxide (10 mg/ml) and injected intraperitoneally in adult mice (> 4 weeks)
487 for postnatal experiments (10 mg/kg) or subcutaneously in pregnant females (E15.5/E16.5) for
488 prenatal experiments (1 mg/kg).

489 All animal experiments were conducted in accordance with the European Commission Council
490 Directive 2010/63/EU (CCD approval AVD1010020172684).

491 HEK293T cell cultures and transfection

492 HEK293T cells were grown in Dulbecco's modified Eagle medium (DMEM; Lonza, Verviers,
493 Belgium) supplemented with 10% fetal bovine serum, 50 U/ml penicillin and 50 µg/ml
494 streptomycin in a 5% CO₂ humidified incubator at 37°. Before transfection, 1 x 10⁵ HEK293T cells
495 were seeded per well of 6-well culture dishes and transfected 24 hours later with expression
496 constructs encoding the *RHEB* variants (0.2 µg), the S6K reporter (0.2 µg), *TSC1* (0.2 µg) and
497 *TSC2* (0.2 µg) using Lipofectamine 2000 (Invitrogen, Carlsbad, CA, USA). To ensure that a total
498 of 0.8 µg plasmid DNA was added per well, empty pcDNA3 vector was included where necessary.
499 The day after transfection, the growth medium was replaced with DMEM without glucose and
500 incubated for a further 4 hours prior to harvesting and western blot analysis.

501 **Western blotting**

502 After transfection, HEK293T cells were transferred on ice, washed with PBS (4 °C) and lysed in
503 70 µl 50 mM Tris-HCl pH 7.6, 100 mM NaCl, 50 mM NaF, 1% Triton X100 in the presence of
504 protease and phosphatase inhibitors (Complete, Roche Molecular Biochemicals, Woerden, The
505 Netherlands). Cell lysates were subjected to immunoblotting using the following primary
506 antibodies: anti-RHEB mouse monoclonal (Groenewoud et al., 2013), anti-TSC1 and TSC2 rabbit
507 polyclonal (Van Slegtenhorst et al., 1998), T389-phosphorylated S6K (1A5, #9206, Cell Signaling
508 Technology), and rabbit anti-myc (#2272, Cell Signaling Technology), all 1:1000. Primary
509 antibody binding was assessed by incubation with goat anti-rabbit (680 nm) and anti-mouse (800
510 nm) conjugates (1:15000, Li-Cor Biosciences, Lincoln, USA) followed by detection on an
511 Odyssey near-infrared scanner (Li-Cor Biosciences).

512 **Neuronal primary hippocampal cultures and transfection**

513 Primary hippocampal neuronal cultures were prepared from FvB/NHsD wild type mice according
514 to the procedure described in (Banker and Goslin, 1988). Neurons were transfected at 1 day *in*

515 *vitro* (DIV1) with the following DNA constructs: control empty vector (1.8 µg per coverslip) and
516 RHEB p.P37L (2.5 µg per coverslip). Plasmids were transfected using Lipofectamine 2000
517 according to the manufacturer's instructions (Invitrogen).

518 **Plasmids**

519 cDNA encoding the *RHEB* (NM_005614.3) c.110C>T (p.P37L) mutation was synthesized by
520 GeneCust. The c.46-47CA>TG (p.S16H) variant was generated by site-directed mutagenesis
521 (Invitrogen) using the following primers: Fw 5' – gcgatcctgggctaccggCAAtgtggggaatcctcatt – 3'
522 and Rev 5' – aatgaggattccccacaTGccggtagcccaggatcgc – 3'. All *RHEB* gene variants were cloned
523 in our dual promoter expression vector using AscI and PacI restriction sites (Reijnders et al., 2017)
524 and the empty vector used as control refers to the dual promoter expression vector without a gene
525 inserted and expressing either tdTOMATO or EGFP (specified in the figures or in the figures'
526 legends). Expression constructs for TSC1, TSC2 and a myc-tagged S6K reporter were as described
527 previously (Dufner Almeida et al., 2019). The following DNA plasmids were obtained from
528 Addgene: pGEMTEZ-TeTxLC (Addgene plasmid #32640; <http://n2t.net/addgene:32640>;
529 RRID:Addgene_32640) (Yu et al., 2004); RV-CAG-DIO-EGFP (Addgene plasmid #87662;
530 <http://n2t.net/addgene:87662>; RRID:Addgene_87662) (Ciceri et al., 2013); pCAG-
531 ERT2CreERT2 (Addgene plasmid #13777; <http://n2t.net/addgene:13777>; RRID:Addgene_13777)
532 (Matsuda and Cepko, 2007); pCAGGS-ChR2-Venus (Addgene plasmid #15753;
533 <http://n2t.net/addgene:15753>; RRID:Addgene_15753) (Petreanu et al., 2007). The TeTxLC was
534 isolated by PCR using the following primers: Fw 5' – taagcagcgcgccaccatgccgatccatcaacaa –
535 3' and Rev 5' – gccatggcgccgcggaattcgcg – 3' and inserted in our dual promoter expression
536 vector using AscI and NotI restriction sites. To generate the loxP-STOP-loxP (LSL) constructs
537 (loxP-STOP-loxP-*RHEB* p.P37L and loxP-STOP-loxP-TeTxLC) the LSL sequence was obtained

538 from the Ai6 CAG-Floxed ZsGreen in Rosa 26 targeting vector (Addgene plasmid #22798;
539 <http://n2t.net/addgene:22798>; RRID:Addgene_22798) using multiple cloning sites and inserted
540 just after the CAGG promoter and before the beginning of the gene in our dual promoter expression
541 vector containing either *RHEB*p.P37L or TeTxLC. The floxed *RHEB* p.P37L construct was
542 generated by introducing two loxP site sequences before the CAGG promoter and at the end of the
543 *RHEB*p.P37L gene, with the same orientation to ensure proper deletion. To achieve this, the
544 following couples of oligonucleotides were used for annealing: Fw 5'-
545 cgcgtATAACTTCGTATAGCATACATTATACGAAGTTATg - 3', Rev: 5'-
546 ctacgATAACTTCGTATAATGTATGCTATACGAAGTTATa - 3'; Fw: 5'-
547 taaATAACTTCGTATAGCATACATTATACGAAGTTATg - 3', Rev: 5'-
548 tcgacATAACTTCGTATAATGTATGCTATACGAAGTTATttaat - 3'.

549 **In utero electroporation**

550 IUE was performed as described previously (Saito and Nakatsuji, 2001). Pregnant FvB/NHsD
551 mice at E14.5 of gestation were used to target the progenitor cells giving rise to pyramidal cells of
552 the layer 2/3. Each *RHEB* DNA construct (including the LSL and floxed conditions) was diluted
553 to a final concentration of 0.5 µg/µl in fast green (0.05%), while other plasmids were diluted to a
554 concentration of 1.5-2 µg/µl. The DNA solution was injected into the lateral ventricle of the
555 embryos while still *in utero*, using a glass pipette controlled by a Picospritzer® III device. When
556 multiple constructs were injected, a mixture of plasmids was prepared to achieve a final
557 concentration of 1.5-2 µg/µl, keeping the *RHEB* concentration constant throughout all the
558 experiments. To ensure proper electroporation of the injected constructs (1-2 µl) into the
559 progenitor cells, five electrical square pulses of 45V with a duration of 50 ms per pulse and 150
560 ms inter-pulse interval were delivered using tweezer-type electrodes connected to a pulse generator

561 (ECM 830, BTX Harvard Apparatus). The positive pole was placed to target the developing
562 somatosensory cortex. Animals of both sexes were used to monitor seizure development, for *ex*
563 *vivo* electrophysiology experiments, or for histological processing with no exclusion criteria
564 determined by a postnatal screening of the targeting area.

565 **Immunostainings**

566 For immunocytochemistry analysis, neuronal cultures were fixed 3 days post-transfection with 4%
567 paraformaldehyde (PFA)/4% sucrose, washed in PBS and incubated overnight at 4°C with primary
568 antibodies in GDB buffer (0.2% BSA, 0.8 M NaCl, 0.5% Triton X-100, 30mM phosphate buffer,
569 pH7.4). Mouse pan anti-SMI312 (1:200, BioLegend, #837904) was used to stain for the axon and,
570 after several washings in PBS, donkey anti-mouse-Alexa488 conjugated was used as secondary
571 antibody diluted in GDB buffer for 1 hour at room temperature (1:200, Jackson ImmunoResearch).
572 Slides were mounted using mowiol-DABCO mounting medium.

573 For the staining of brain tissue sections, mice were deeply anesthetized with an overdose
574 of Nembutal and transcardially perfused with 4% PFA in PB. Brains were extracted and post-fixed
575 for 1 hour in 4% PFA. They were then embedded in gelatin and cryoprotected in 30% sucrose in
576 0.1 M Phosphate Buffer (PB) overnight, frozen on dry ice, and sectioned using a freezing
577 microtome (40 µm thick). Immunofluorescence was performed on free-floating sections that were
578 first washed multiple times in PBS and blocked in 10% normal horse serum (NHS) and 0.5%
579 Triton X-100 in PBS for 1 hour at room temperature. Primary antibodies diluted in PBS containing
580 2% NHS and 0.5% Triton X-100 were added at room temperature overnight. The day after,
581 sections were washed three times with PBS and secondary antibodies were added diluted in PBS
582 containing 2% NHS and 0.5% Triton X-100. After washing in PBS and 0.05 M PB, sections were
583 counterstained with 4',6-diamidino-2-phenylindole solution (DAPI, 1:10000, Invitrogen) before

584 being washed in PB 0.05 M and mounted on slides using chromium (3) potassium sulfate
585 dodecahydrate (Sigma-Aldrich) and left to dry. Finally, sections were mounted on glass with
586 mowiol (Sigma-Aldrich).

587 Biocytin labelling was achieved by fixating the patched slices overnight in 4% PFA in PB
588 at 4°. Slices were then washed multiple times in PBS and incubated with Alexa488-Streptavidin
589 (1:200; #016-540-084, Jackson ImmunoResearch) or AlexaCy5-Streptavidin (1:200; #016-170-
590 084, Jackson ImmunoResearch) overnight at 4°. The next day, after washing in PBS and 0.05 M
591 PB, sections were counterstained with DAPI (1:10000, Invitrogen) and mounted on glass with
592 mowiol (Sigma-Aldrich).

593 When performing Nissl stainings, few selected free floating sections corresponding to the
594 Somatosensory cortex were mounted on glass using chromium (3) potassium sulfate
595 dodecahydrate (Sigma-Aldrich) and left to dry overnight. Slides were stained in 0.1 % Cresyl
596 Violet for 4-10 minutes, then rinsed briefly in tap water to remove excess stain, dehydrated in
597 increasing percentages of alcohol, cleared with xylene and covered using Permount (Fisher
598 Scientific).

599 The primary antibodies used in this study to stain for the specific targets indicated for each
600 experiment in the figures' legends were: anti-rabbit pS6 (Ser 240/244), 1:1000; Cell signaling,
601 catalog #5634; anti-rabbit RFP, 1:2000; Rockland, catalog 600-401-379; anti-rabbit RHEB,
602 1:1000, Proteintech Group Inc., catalog 15924-1-AP; anti-rabbit CUX1, 1:1000; Proteintech
603 Group Inc., catalog 11733-1-AP; anti-rat CTIP2, 1:200; Abcam, catalog ab18465; anti-rabbit
604 NeuN, 1:2000; Millipore catalog ABN78 (RRID: AB_10807945); anti-mouse SATB2, 1:1000;
605 Santa cruz, catalog sc-81376; anti-rabbit synapsin 1, 1:1000; Merck Millipore, catalog #AB1543P;
606 anti-guinea pig VGLUT1, 1:1000; Merck Millipore, catalog #AB5905; Secondary antibodies used

607 were: donkey anti rabbit 488, catalog #711-545-152; donkey anti rabbit 647, catalog #711-605-
608 152; donkey anti rabbit Cy3, catalog #711-165-152; donkey anti mouse 488, catalog #715-545-
609 150; donkey anti mouse 647, catalog #715-605-150; donkey anti rat Cy5, catalog #712-175-150;
610 donkey anti guinea pig 647, catalog #706-605-148; all from Jackson ImmunoResearch, 1:200.

611 **LFP and EEG recordings**

612 Starting from 3 weeks of age surgeries were performed according to the procedures described in
613 (Koene et al., 2019; Kool et al., 2019). After at least three days of recovery from the EEG surgical
614 procedure, mice were connected to a wireless EEG recorder (NewBehavior, Zurich, Switzerland)
615 for 24 hours per day for at least two consecutive days (one session of recordings). EEG recordings
616 were manually assessed by two different researchers blind for the genotypes to check for
617 occurrence of seizures, defined as a pattern of repetitive spike discharges followed by a progressive
618 evolution in spike amplitude with a distinct post-ictal depression phase, based on the criteria
619 described in (Kane et al., 2017). If no seizures were detected during the first week *post-surgery*,
620 mice were recorded for another session of 48-56 hr for a maximum of four sessions over four
621 weeks *post-surgery*. During the days in which no EEG recordings were performed, mice were
622 monitored daily to assess for the presence of behavioural seizures and discomfort.

623 For the LFP recordings, two days after the surgical procedure, mice were head-fixed to a
624 brass bar suspended over a cylindrical treadmill to allow anaesthesia-free recording sessions and
625 placed in a light-isolated Faraday cage as described in (Kool et al., 2019). Mice were allowed to
626 habituate to the set-up before proceeding to the recording. LFP measurements were acquired every
627 day in sessions of 20-30' for five or eight consecutive days, using the Open Ephys platform with
628 a sampling rate of 3 kS/s and a band pass filter between 0.1 and 200 Hz. For the power spectrum
629 analysis, the average power density spectrum of all the days of recording was obtained using

630 MATLAB software (MathWorks; RRID:SCR_001622). The mean relative power was calculated
631 over four frequency bands relative to the total power: delta (2–4 Hz), theta (4–8 Hz), beta (13–30
632 Hz), and gamma (30–50 Hz).

633 At the end of each experiment, mice were sacrificed for immunohistological analysis to
634 assess electrodes' positioning, amount of targeting and efficiency of cre-dependent recombination
635 when tamoxifen was administered.

636 ***Ex vivo* slice electrophysiology for excitability**

637 P21-P25 mice of both sexes *in utero* electroporated with the plasmids specified in the figures and
638 in the legends for each experiment were anaesthetized with isoflurane before decapitation. The
639 brain was quickly removed and submerged in ice cold cutting solution containing (in mM): 110
640 Choline Chloride, 2.5 KCl, 1.2 NaH₂PO₄, 26 NaHCO₃, 25 D-glucose, 0.5 CaCl₂, 10 MgSO₄. Acute
641 300 µm coronal slices were made of the somatosensory cortex using a vibratome (HM650V,
642 Microm) while being saturated with 95% O₂/5% CO₂. The slices were immediately transferred to
643 a submerged slice holding chamber and incubated at ±34°C for 5 min before being transferred to
644 a second slice holding chamber also kept at ±34°C. The second holding chamber contained the
645 same artificial cerebrospinal fluid (ACSF) as was used during all recordings and contained (in
646 mM): 125 NaCl, 3 KCl, 1.25 NaH₂PO₄, 26 NaHCO₃, 10 glucose, 2 CaCl₂, 1 MgSO₄. During the
647 slicing procedure and experimental recordings, slices were saturated with 95% O₂/5% CO₂. Slices
648 recovered for an hour at room temperature before starting the experiment. After the experiment,
649 slices were fixed in 4% PFA overnight and then transferred to PBS until further processing. Whole-
650 cell patch clamp recordings were obtained from the soma of visually identified L2/L3 pyramidal
651 neurons from the S1 cortex with an upright microscope using IR-DIC optics (BX51WI, Olympus,
652 Tokyo, Japan). Targeted cells in the ipsilateral side were identified by the presence of either

653 tdTomato or GFP, depending on the experiment, elicited by an Olympus U-RFL-T burner. All
654 recordings were done under physiological temperatures of 30 ± 1 °C. Patch clamp pipettes were
655 pulled from standard wall filament borosilicate glass to obtain electrodes with a tip resistance
656 between 2-4 M Ω . All recordings were performed using a Multiclamp 700B (Molecular Devices,
657 Sunnyvale, CA, USA) and digitized by a Digidata 1440A (Molecular Devices, Sunnyvale, CA,
658 USA). For the current clamp recordings, pipets were filled with a K-gluconate internal solution
659 containing (in mM): 125 K-gluconate, 10 NaCl, 10 HEPES, 0.2 EGTA, 4.5 MgATP, 0.3 NaGTP
660 and 10 Na-phosphocreatine. For analysis of cell morphology, biocytin (5%) was added to the
661 intracellular solution. The final solution was adjusted to a pH of 7.2–7.4 using KOH and had an
662 osmolarity of 280 ± 3 . After getting a seal of at least 1 G Ω , whole cell configuration was obtained
663 by applying brief negative pressure together with a short electric pulse. Prior to breaking in, cell
664 capacitance was compensated. Series resistance was monitored but not corrected. Recordings with
665 an unstable series resistance and higher than 20 M Ω were rejected. Membrane potentials were not
666 corrected for liquid junction potential. Resting membrane potential was measured immediately
667 after break in.

668 Each sweep started with a small and short hyperpolarizing step (-50 pA, 50 ms) to monitor
669 access resistance. Action potentials were triggered by square step current injections into the
670 patched neurons while holding them at -70 mV. Steps were 750 ms long and started at -300 pA
671 with increments of 20 pA. The number of action potentials and action potential properties were
672 analyzed using Clampfit 10.7.0.3 (Molecular Devices, LLC, USA). For each cell, the first action
673 potential at rheobase was analyzed. The threshold was calculated by plotting the first derivative of
674 the trace. The threshold was defined when the first derivative was lower than 10 mV/ms. Series
675 resistance was calculated offline for each cell by plotting the difference in voltages between

676 baseline and the hyperpolarizing steps. A linear line was plotted to visualize passive current only.
677 The tau was calculated by fitting a standard exponential on the end of the hyperpolarizing steps.
678 From tau and series resistance, capacitance was calculated.

679

680 ***Ex vivo* slice electrophysiology for optogenetics**

681 P21-P25 mice of both sexes *in utero* electroporated either with the RHEBp.P37L and pCAGGS-
682 ChR2-Venus plasmids or the empty vector and pCAGGS-ChR2-Venus plasmids (Petreanu et al.,
683 2007), were anaesthetized with isoflurane before decapitation. The brain was quickly removed and
684 submerged in ice cold cutting solution containing (in mM): 93 NMDG, 93 HCl, 2.5 KCl, 1.2
685 NaHPO₄, 30 NaHCO₃, 25 glucose, 20 HEPES, 5 Na-ascorbate, 3 Na-pyruvate, 2 Thiourea, 10
686 MgSO₄, 0.5 CaCl₂, 5 N-acetyl-L-Cysteine (osmolarity 310 ± 5; bubbled with 95% O₂ / 5% CO₂)
687 (Ting et al., 2014). Next, 250 µm thick coronal slices were cut using a Leica vibratome (VT1000S).
688 For the recovery, brain slices were incubated for 5 min in slicing medium at 34 ± 1°C and
689 subsequently for ~40 min in ACSF (containing in mM: 124 NaCl, 2.5 KCl, 1.25 Na₂HPO₄, 2
690 MgSO₄, 2 CaCl₂, 26 NaHCO₃, and 20 D-glucose, osmolarity 310 ± 5mOsm; bubbled with 95%
691 O₂ / 5% CO₂) at 34 ± 1°C. After recovery brain slices were stored at room temperature. For all
692 recordings, slices were bathed in 34 ± 1°C ACSF (bubbled with 95% O₂ / 5% CO₂). Whole-cell
693 patch-clamp recordings were recorded with an EPC-10 amplifier (HEKA Electronics, Lambrecht,
694 Germany) and sampled at 20 kHz. Resting membrane potential and input resistance were recorded
695 after whole-cell configuration was reached. Recordings were excluded if the series resistance or
696 input resistance (RS) varied by >25% over the course of the experiment. Voltage and current clamp
697 recordings were performed using borosilicate glass pipettes with a resistance of 3-5 MΩ that was
698 filled with K-gluconate-based internal solution (in mM: 124 K-gluconate, 9 KCl, 10 KOH, 4 NaCl,

699 10 HEPES, 28.5 sucrose, 4 Na₂ATP, 0.4 Na₃GTP (pH 7.25-7.35; osmolarity 290 ± 5mOsm)).
700 Recording pipettes were supplemented with 1 mg/ml biocytin to check the location of the patched
701 cells with histological staining. Current clamp recordings were corrected offline for the calculated
702 liquid junction potential of -10.2 mV.

703 Full-field optogenetic stimulation (470 nm peak excitation) was generated by the use of a
704 TTL-pulse controlled pE2 light emitting diode (CoolLED, Andover, UK). Light intensities at 470
705 nm were recorded using a photometer (Newport 1830-C equipped with an 818-ST probe, Irvine,
706 CA) at the level of the slice. To trigger neurotransmitter release from targeted axons we delivered
707 a 1 ms light pulse with an intensity of 99.8 mW/mm² at a frequency of 0.1 Hz. To ensure that we
708 recorded action potential-driven neurotransmitter release most experiments were concluded by
709 bath application of 10 μM tetrodotoxin (TTX), which blocked all post-synaptic responses in the
710 recorded pyramidal neurons.

711

712 **Imaging and analysis**

713 Images of Nissl stained sections were acquired in brightfield with a Nanozoomer scanner
714 (Hamamatsu, Bridgewater, NJ) at a 40X resolution using the NDP.view2 software. All
715 immunofluorescent images were acquired using a LSM700 confocal microscope (Zeiss). For the
716 analysis of the axons *in vitro*, at least ten distinct confocal images from two different neuronal
717 batches were taken from each coverslip for each experiment (20X objective, 0.5 zoom, 1024x1024
718 pixels; neurons were identified by the red immunostaining signal). The simple neurite tracer plugin
719 from the FIJI ImageJ software was used for the analysis of the axonal length and branches.
720 Overview images of the coronal sections were acquired by tile scan with a 10X objective. Zoom
721 in images of the targeted area (ipsilateral) and contralateral S1 were taken using a 10X objective.
722 For the migration analysis, confocal images (10X objective, 0.5 zoom, 1024x1024 pixels) were

723 taken from 2 – 3 non-consecutive sections from at least 2/3 electroporated animals per condition.
724 Images were rotated to correctly position the cortical layers, and the number of cells in different
725 layers were counted using the ‘analyze particles’ plugin of FIJI. The results were exported to a
726 spreadsheet for further analysis. Cortical areas from the pia to the ventricle were divided into 10
727 bins of equal size and the percentage of tdTomato-positive cells per bin was calculated. The soma
728 size analysis was performed on z-stacks images acquired using a 20X objective, 1 zoom,
729 1024x1024 pixels, of the targeted cells in both empty vector control and *RHEBp.P37L* coronal
730 sections. A ROI around each targeted cell in maximum intensity projection pictures was defined
731 using the FIJI software and the area of the soma was measured using the ‘Measure’ option in
732 ImageJ. For the analysis of pS6 intensity levels, confocal images (10X objective, 0.5 zoom,
733 1024x1024 pixels) of the ipsilateral and contralateral S1 cortex were acquired with the same master
734 gain from both control and RHEB groups previously stained together against pS6 (240/244). The
735 overall intensity level of the staining for each picture was measured using the ‘RGB measure’
736 plugin of FIJI and the values of each ipsilateral side were normalized against the corresponding
737 contralateral side and plotted as averaged values. The analysis of the fluorescent intensity of the
738 axonal branches over the contralateral cortical layers, was obtained from 3-4 matched coronal
739 sections from at least 3 different animals per group with comparable amount of targeting. The
740 axonal arborization was measured selecting the S1/S2 border, drawing a straight segmented line
741 with adjusted width and length and resized in 1000 bins, and using the ‘plot profile’ option of the
742 analyze section of FIJI to measure the fluorescent intensity of the tdTomato signal over the
743 different layers. The values obtained for each section were exported to a spreadsheet were they
744 were normalized against the mean background fluorescent intensity calculated on a non-targeted,
745 cortical area of fixed size and plotted as averaged values over 10 bins of equal size. For the analysis

746 of the morphology of biocytin filled pyramidal cells and ectopic cells in the nodule labelled with
747 streptavidin-488 or streptavidin-Cy5, z-stacks images were taken using a 20X objective, 0.5 zoom,
748 1024x1024 pixels, to include the dendritic tree. Maximum intensity projection pictures were
749 analyzed using the SynD software for the MATLAB platform to automatically detect the dendritic
750 morphology and perform Sholl analysis (Schmitz et al., 2011).

751

752 **Statistics**

753 Normality of the distribution for the different experiments was determined using either the Wilk-
754 Shapiro test (Figures 1A, 1C, 2D, 3E-F, 4B, 5A, 6B, 8F and Supplementary Figure 5B,) or the
755 Kolmogorov-Smirnov test (Figures 2A, 2B, 5C, 8B-C-E). Statistical analysis was performed using
756 a one-way ANOVA (or corresponding non-parametric Kruskal-Wallis test), two-way repeated-
757 measures ANOVA or mixed-effects analysis, Student's t test (or corresponding non-parametric
758 Mann-Whitney test) and correlation/association analysis. The specific test used for each
759 experiment and relative significance are specified in the figures' legends, in the supplementary
760 tables or in the results section (when data are not shown in a figure). For all statistical analyses α
761 was set at 0.05. Values are represented as average \pm SEM or as median, minimum and maximum
762 values (specified in the figures' legends). No samples or mice were excluded from the final
763 analysis. Group sizes, biological replicates, number of cells, samples or brain sections are indicated
764 in the figures and their corresponding legends. All statistical tests were performed either using
765 GraphPad Prism 8.0 (RRID: SCR_002798) or SPSS Statistics v25.0 (RRID:SCR_002865).

766

767

768 **ACKNOWLEDGMENTS**

769 The authors would like to thank Charlotte de Konink, Hang Le Ha, Anne Polman and Chi Yeung
770 for their technical contribution and Minetta Elgersma-Hooisma for managing the mouse colony.
771 We also would like to thank Enzo Nio for advice regarding the code used to analyze the data and
772 Steven Kushner and Dick Jaarsma for fruitful discussions. This work was supported by the Dutch
773 TSC foundation (STSN) (G.M.v.W) and the Dutch Epilepsy foundation (Epilepsie fonds) (Y.E.).

774 **COMPETING INTERESTS**

775 The authors declare no competing interests.

776 **AUTHOR CONTRIBUTIONS**

777 Conceptualization, M.P.O., Y.E. and G.M.v.W.; Methodology, M.P.O. , Y.E. and G.M.v.W.;
778 Investigation, M.P.O., L.M.C.K., C.B.S., M.N.; Formal Analysis: M.P.O., L.M.C.K., C.B.S.,
779 M.N.; Software, M.d.B.v.V.; Writing – Original Draft: M.P.O. and G.M.v.W.; Writing – Review
780 & Editing: M.P.O., L.M.C.K., C.B.S., M.N., M.d.B.v.V., Z.G., Y.E., G.M.v.W.; Visualization:
781 M.P.O.; Supervision: G.M.v.W.; Funding Acquisition: Y.E. and G.M.v.W.

782 **REFERENCES**

- 783 Abs E, Goorden SMI, Schreiber J, Overwater IE, Hoogeveen-Westerveld M, Bruinsma CF,
784 Aganović E, Borgesius NZ, Nellist M, Elgersma Y. 2013. TORC1-dependent epilepsy
785 caused by acute biallelic Tsc1 deletion in adult mice. *Ann Neurol* **74**:569–79.
786 doi:10.1002/ana.23943
- 787 Bai X, Ma D, Liu A, Shen X, Wang QJ, Liu Y, Jiang Y. 2007. Rheb activates mTOR by
788 antagonizing its endogenous inhibitor, FKBP38. *Science* **318**:977–80.
789 doi:10.1126/science.1147379
- 790 Banker G, Goslin K. 1988. Developments in neuronal cell culture. *Nature*.
791 doi:10.1038/336185a0
- 792 Barkovich AJ, Guerrini R, Kuzniecky RI, Jackson GD, Dobyns WB. 2012. A developmental and
793 genetic classification for malformations of cortical development: Update 2012. *Brain*.
794 doi:10.1093/brain/aws019
- 795 Bhaskar PT, Hay N. 2007. The Two TORCs and Akt. *Dev Cell*.
796 doi:10.1016/j.devcel.2007.03.020
- 797 Binder DK, Croll SD, Gall CM, Scharfman HE. 2001. BDNF and epilepsy: Too much of a good
798 thing? *Trends Neurosci*. doi:10.1016/S0166-2236(00)01682-9
- 799 Budnik V, Ruiz-Cañada C, Wendler F. 2016. Extracellular vesicles round off communication in
800 the nervous system. *Nat Rev Neurosci* **17**:160–172. doi:10.1038/nrn.2015.29
- 801 Chassoux F, Landre E, Rodrigo S, Beuvon F, Turak B, Semah F, Devaux B. 2008. Intralesional
802 recordings and epileptogenic zone in focal polymicrogyria. *Epilepsia* **49**:51–64.

- 803 doi:10.1111/j.1528-1167.2007.01267.x
- 804 Chauvière L, Rafrafi N, Thinus-Blanc C, Bartolomei F, Esclapez M, Bernard C. 2009. Early
805 deficits in spatial memory and theta rhythm in experimental temporal lobe epilepsy. *J*
806 *Neurosci* **29**:5402–5410. doi:10.1523/JNEUROSCI.4699-08.2009
- 807 Chevassus-au-Louis N, Baraban SC, Gaíarsa J-L, Ben-Ari Y. 1999. Cortical Malformations and
808 Epilepsy: New Insights from Animal Models. *Epilepsia* **40**:811–821. doi:10.1111/j.1528-
809 1157.1999.tb00786.x
- 810 Choi Y-J, Di Nardo A, Kramvis I, Meikle L, Kwiatkowski DJ, Sahin M, He X. 2008. Tuberous
811 sclerosis complex proteins control axon formation. *Genes Dev* **22**:2485–95.
812 doi:10.1101/gad.1685008
- 813 Ciceri G, Dehorter N, Sols I, Huang ZJ, Maravall M, Marín O. 2013. Lineage-specific laminar
814 organization of cortical GABAergic interneurons. *Nat Neurosci* **16**:1199–1210.
815 doi:10.1038/nn.3485
- 816 Crino PB. 2011. mTOR: A pathogenic signaling pathway in developmental brain malformations.
817 *Trends Mol Med* **17**:734–742. doi:10.1016/j.molmed.2011.07.008
- 818 Dufner Almeida LG, Nanhoe S, Zonta A, Hosseinzadeh M, Kom-Gortat R, Elfferich P, Schaaf
819 G, Kenter A, Kümmel D, Migone N, Povey S, Ekong R, Nellist M. 2019. Comparison of
820 the functional and structural characteristics of rare TSC2 variants with clinical and genetic
821 findings. *Hum Mutat* humu.23963. doi:10.1002/humu.23963
- 822 Fader CM, Sánchez DG, Mestre MB, Colombo MI. 2009. TI-VAMP/VAMP7 and
823 VAMP3/cellubrevin: two v-SNARE proteins involved in specific steps of the

- 824 autophagy/multivesicular body pathways. *Biochim Biophys Acta - Mol Cell Res* **1793**:1901–
825 1916. doi:10.1016/j.bbamcr.2009.09.011
- 826 Fame RM, MacDonald JL, Macklis JD. 2011. Development, specification, and diversity of
827 callosal projection neurons. *Trends Neurosci*. doi:10.1016/j.tins.2010.10.002
- 828 Fenlon LR, Suárez R, Richards LJ. 2017. The anatomy, organisation and development of
829 contralateral callosal projections of the mouse somatosensory cortex. *Brain Neurosci Adv*
830 **1**:239821281769488. doi:10.1177/2398212817694888
- 831 Gaisano HY, Sheu L, Foskett JK, Trimble WS. 1994. Tetanus toxin light chain cleaves a vesicle-
832 associated membrane protein (VAMP) isoform 2 in rat pancreatic zymogen granules and
833 inhibits enzyme secretion. *J Biol Chem* **269**:17062–17066.
- 834 Gong X, Zhang L, Huang T, Lin T V., Miyares L, Wen J, Hsieh L, Bordey A. 2015. Activating
835 the translational repressor 4E-BP or reducing S6K-GSK3 β activity prevents accelerated
836 axon growth induced by hyperactive mTOR *in vivo*. *Hum Mol Genet* **24**:5746–5758.
837 doi:10.1093/hmg/ddv295
- 838 Goorden SMI, Abs E, Bruinsma CF, Riemsdijk FW, van Woerden GM, Elgersma Y. 2015.
839 Intact neuronal function in Rheb1 mutant mice: implications for TORC1-based treatments.
840 *Hum Mol Genet* **24**:3390–8. doi:10.1093/hmg/ddv087
- 841 Groenewoud MJ, Goorden SMI, Kassies J, Pellis-van Berkel W, Lamb RF, Elgersma Y,
842 Zwartkruis FJT. 2013. Mammalian target of rapamycin complex I (mTORC1) activity in ras
843 homologue enriched in brain (Rheb)-deficient mouse embryonic fibroblasts. *PLoS One*
844 **8**:e81649. doi:10.1371/journal.pone.0081649

- 845 Hanai S, Sukigara S, Dai H, Owa T, Horike S ichi, Otsuki T, Saito T, Nakagawa E, Ikegaya N,
846 Kaido T, Sato N, Takahashi A, Sugai K, Saito Y, Sasaki M, Hoshino M, Goto Y ichi,
847 Koizumi S, Itoh M. 2017. Pathologic Active mTOR Mutation in Brain Malformation with
848 Intractable Epilepsy Leads to Cell-Autonomous Migration Delay. *Am J Pathol* **187**:1177–
849 1185. doi:10.1016/j.ajpath.2017.01.015
- 850 Hsieh LS, Wen JH, Claycomb K, Huang Y, Harrsch FA, Naegele JR, Hyder F, Buchanan GF,
851 Bordey A. 2016. Convulsive seizures from experimental focal cortical dysplasia occur
852 independently of cell misplacement. *Nat Commun* **7**:11753. doi:10.1038/ncomms11753
- 853 Juric-Sekhar G, Hevner RF. 2019. Malformations of Cerebral Cortex Development: Molecules
854 and Mechanisms. *Annu Rev Pathol Mech Dis* **14**:293–318. doi:10.1146/annurev-
855 pathmechdis-012418-012927
- 856 Kane N, Acharya J, Benickzy S, Caboclo L, Finnigan S, Kaplan PW, Shibasaki H, Pressler R,
857 van Putten MJAM. 2017. A revised glossary of terms most commonly used by clinical
858 electroencephalographers and updated proposal for the report format of the EEG findings.
859 Revision 2017. *Clin Neurophysiol Pract* **2**:170–185. doi:10.1016/j.cnp.2017.07.002
- 860 Koene LMC, van Grondelle SE, Proietti Onori M, Wallaard I, Kooijman NHRM, van Oort A,
861 Schreiber J, Elgersma Y. 2019. Effects of antiepileptic drugs in a new TSC/mTOR-
862 dependent epilepsy mouse model. *Ann Clin Transl Neurol* **6**:1273–1291.
863 doi:10.1002/acn3.50829
- 864 Kool MJ, Proietti Onori M, Borgesius NZ, van de Bree JE, Elgersma-Hooisma M, Nio E,
865 Bezstarosti K, Buitendijk GHS, Aghadavoud Jolfaei M, Demmers JAA, Elgersma Y, van
866 Woerden GM. 2019. CAMK2-dependent signaling in neurons is essential for survival. *J*

- 867 *Neurosci* 1341–18. doi:10.1523/jneurosci.1341-18.2019
- 868 Krueger DA, Sadhwani A, Byars AW, de Vries PJ, Franz DN, Whittemore VH, Filip-Dhima R,
869 Murray D, Kapur K, Sahin M. 2017. Everolimus for treatment of tuberous sclerosis
870 complex-associated neuropsychiatric disorders. *Ann Clin Transl Neurol* **4**:877–887.
871 doi:10.1002/acn3.494
- 872 Laplante M, Sabatini DM. 2012. mTOR Signaling. *Cold Spring Harb Perspect Biol* **4**:a011593-
873 doi:10.1101/cshperspect.a011593
- 874 Leventer RJ, Guerrini R, Dobyns WB. 2008. Malformations of cortical development and
875 epilepsy. *Dialogues Clin Neurosci*.
- 876 Leventer RJ, Phelan EM, Coleman LT, Kean MJ, Jackson GD, Harvey AS. 1999. Clinical and
877 imaging features of cortical malformations in childhood. *Neurology* **53**:715–22.
878 doi:10.1212/wnl.53.4.715
- 879 Li Y, Inoki K, Guan K-L. 2004. Biochemical and Functional Characterizations of Small GTPase
880 Rheb and TSC2 GAP Activity. *Mol Cell Biol* **24**:7965–7975. doi:10.1128/mcb.24.18.7965-
881 7975.2004
- 882 Lim JS, Kim W, Kang H-C, Kim SH, Park AH, Park EK, Cho Y-W, Kim S, Kim HM, Kim JA,
883 Kim J, Rhee H, Kang S-G, Kim HD, Kim D, Kim D-S, Lee JH. 2015. Brain somatic
884 mutations in MTOR cause focal cortical dysplasia type II leading to intractable epilepsy.
885 *Nat Med* **21**:395–400. doi:10.1038/nm.3824
- 886 Major P, Rakowski S, Simon M V., Cheng ML, Eskandar E, Baron J, Leeman BA, Frosch MP,
887 Thiele EA. 2009. Are cortical tubers epileptogenic? Evidence from electrocorticography.

- 888 *Epilepsia* **50**:147–154. doi:10.1111/j.1528-1167.2008.01814.x
- 889 Manning BD, Cantley LC. 2003. Rheb fills a GAP between TSC and TOR. *Trends Biochem Sci*.
890 doi:10.1016/j.tibs.2003.09.003
- 891 Matsuda T, Cepko CL. 2007. Controlled expression of transgenes introduced by in vivo
892 electroporation. *Proc Natl Acad Sci U S A* **104**:1027–32. doi:10.1073/pnas.0610155104
- 893 Milikovsky DZ, Weissberg I, Kamintsky L, Lippmann K, Schefenbauer O, Frigerio F, Rizzi M,
894 Sheintuch L, Zelig D, Ofer J, Vezzani A, Friedman A. 2017. Electrographic
895 dynamics as a novel biomarker in five models of epileptogenesis. *J Neurosci* **37**:4450–4461.
896 doi:10.1523/JNEUROSCI.2446-16.2017
- 897 Moffat JJ, Ka M, Jung EM, Kim WY. 2015. Genes and brain malformations associated with
898 abnormal neuron positioning. *Mol Brain* **8**:1–12. doi:10.1186/s13041-015-0164-4
- 899 Nie D, Di Nardo A, Han JM, Baharanyi H, Kramvis I, Huynh T, Dabora S, Codeluppi S,
900 Pandolfi PP, Pasquale EB, Sahin M. 2010. Tsc2-Rheb signaling regulates EphA-mediated
901 axon guidance. *Nat Neurosci* **13**:163–72. doi:10.1038/nn.2477
- 902 Overwater IE, Rietman AB, Bindels-De Heus K, Looman CWN, Rizopoulos D, Sibindi TM,
903 Cherian PJ, Jansen FE, Moll HA, Elgersma Y, De Wit MCY. 2016. Sirolimus for epilepsy
904 in children with tuberous sclerosis complex. *Neurology* **87**:1011–1018.
905 doi:10.1212/WNL.0000000000003077
- 906 Overwater Iris E., Rietman AB, Mous SE, Bindels-De Heus K, Rizopoulos D, Ten Hoopen LW,
907 Van Der Vaart T, Jansen FE, Elgersma Y, Moll HA, De Wit MCY. 2019. A randomized
908 controlled trial with everolimus for IQ and autism in tuberous sclerosis complex. *Neurology*

- 909 **93**:E200–E209. doi:10.1212/WNL.0000000000007749
- 910 Overwater Iris E, Rietman AB, van Eeghen AM, de Wit MCY. 2019. Everolimus for the
911 treatment of refractory seizures associated with tuberous sclerosis complex (TSC): current
912 perspectives. *Ther Clin Risk Manag* **15**:951–955. doi:10.2147/TCRM.S145630
- 913 Park SM, Lim JS, Ramakrishna S, Kim SH, Kim WK, Lee JHJ, Kang H-C, Reiter JF, Kim DS,
914 Kim H (Henry), Lee JHJ. 2018. Brain somatic mutations in MTOR disrupt neuronal
915 ciliogenesis, leading to focal cortical dyslamination. *Neuron* **99**:1–15.
916 doi:<http://dx.doi.org/10.1016>
- 917 Parmar N, Tamanoi F. 2010. Rheb G-proteins and the activation of mTORC1 *The Enzymes*.
918 Academic Press. pp. 39–56. doi:10.1016/S1874-6047(10)27003-8
- 919 Patel B, Patel J, Cho J-H, Manne S, Bonala S, Henske E, Roegiers F, Markiewski M,
920 Karbowiczek M. 2015. Exosomes mediate the acquisition of the disease phenotypes by
921 cells with normal genome in tuberous sclerosis complex. *Oncogene* 1–10.
922 doi:10.1038/onc.2015.358
- 923 Petreanu L, Huber D, Sobczyk A, Svoboda K. 2007. Channelrhodopsin-2-assisted circuit
924 mapping of long-range callosal projections. *Nat Neurosci* **10**:663–668. doi:10.1038/nn1891
- 925 Reijnders MRF, Kousi M, Van Woerden GMM, Klein M, Bralten J, Mancini GMS, Van
926 Essen T, Proietti-Onori M, Smeets EEJEJ, Van Gastel M, Stegmann APAPA, Stevens
927 SJCJC, Lelieveld SHH, Gilissen C, Pfundt R, Tan PLL, Kleefstra T, Franke B, Elgersma Y,
928 Katsanis N, Brunner HGG. 2017. Variation in a range of mTOR-related genes associates
929 with intracranial volume and intellectual disability. *Nat Commun* **8**:1052.

- 930 doi:10.1038/s41467-017-00933-6
- 931 Represa A. 2019. Why Malformations of Cortical Development Cause Epilepsy. *Front Neurosci*
- 932 **13**:250. doi:10.3389/fnins.2019.00250
- 933 Ribierre T, Deleuze C, Bacq A, Baldassari S, Marsan E, Chipaux M, Muraca G, Roussel D,
- 934 Navarro V, Leguern E, Miles R, Baulac S. 2018. Second-hit mosaic mutation in mTORC1
- 935 repressor DEPDC5 causes focal cortical dysplasia-associated epilepsy. *J Clin Invest*
- 936 **128**:2452–2458. doi:10.1172/JCI99384
- 937 Sabatini DM. 2017. Twenty-five years of mTOR: Uncovering the link from nutrients to growth.
- 938 *Proc Natl Acad Sci U S A*. doi:10.1073/pnas.1716173114
- 939 Saito T, Nakatsuji N. 2001. Efficient gene transfer into the embryonic mouse brain using in vivo
- 940 electroporation. *Dev Biol* **240**:237–46. doi:10.1006/dbio.2001.0439
- 941 Saxton RA, Sabatini DM. 2017. mTOR Signaling in Growth, Metabolism, and Disease. *Cell*.
- 942 doi:10.1016/j.cell.2017.02.004
- 943 Schiavo GG, Benfenati F, Poulain B, Rossetto O, De Laureto PP, Dasgupta BR, Montecucco C.
- 944 1992. Tetanus and botulinum-B neurotoxins block neurotransmitter release by proteolytic
- 945 cleavage of synaptobrevin. *Nature* **359**:832–835. doi:10.1038/359832a0
- 946 Schmitz SK, Hjorth JJJ, Joemai RMS, Wijntjes R, Eijgenraam S, de Bruijn P, Georgiou C, de
- 947 Jong APH, van Ooyen A, Verhage M, Cornelisse LN, Toonen RF, Veldkamp W. 2011.
- 948 Automated analysis of neuronal morphology, synapse number and synaptic recruitment. *J*
- 949 *Neurosci Methods* **195**:185–193. doi:10.1016/j.jneumeth.2010.12.011
- 950 Shimojo M, Courchet J, Pieraut S, Torabi-Rander N, Sando R, Polleux F, Maximov A. 2015.

- 951 SNAREs Controlling Vesicular Release of BDNF and Development of Callosal Axons. *Cell*
952 *Rep* **11**:1054–1066. doi:10.1016/j.celrep.2015.04.032
- 953 Ting JT, Daigle TL, Chen Q, Feng G. 2014. Acute brain slice methods for adult and aging
954 animals: Application of targeted patch clamp analysis and optogenetics. *Methods Mol Biol*
955 **1183**:221–242. doi:10.1007/978-1-4939-1096-0_14
- 956 Tsai PT, Greene-Colozzi E, Goto J, Anderl S, Kwiatkowski DJ, Sahin M. 2013. Prenatal
957 rapamycin results in early and late behavioral abnormalities in wildtype C57BL/6 mice.
958 *Behav Genet* **43**:51–9. doi:10.1007/s10519-012-9571-9
- 959 Van Slegtenhorst M, Nellist M, Nagelkerken B, Cheadle J, Snell R, Van Den Ouweland A,
960 Reuser A, Sampson J, Halley D, Van Der Sluijs P. 1998. Interaction between hamartin and
961 tuberin, the TSC1 and TSC2 gene products. *Hum Mol Genet* **7**:1053–1057.
962 doi:10.1093/hmg/7.6.1053
- 963 Wang C-L, Zhang L, Zhou Y, Zhou J, Yang X-J, Duan S, Xiong Z-Q, Ding Y-Q. 2007. Activity-
964 dependent development of callosal projections in the somatosensory cortex. *J Neurosci*
965 **27**:11334–42. doi:10.1523/JNEUROSCI.3380-07.2007
- 966 Way SW, Rozas NS, Wu HC, Mckenna J, Reith RM, Hashmi SS, Dash PK, Gambello MJ. 2012.
967 The differential effects of prenatal and/or postnatal rapamycin on neurodevelopmental
968 defects and cognition in a neuroglial mouse model of tuberous sclerosis complex. *Hum Mol*
969 *Genet* **21**:3226–3236. doi:10.1093/hmg/dds156
- 970 Wong M, Roper SN. 2016. Genetic animal models of malformations of cortical development and
971 epilepsy. *J Neurosci Methods*. doi:10.1016/j.jneumeth.2015.04.007

972 Yan L, Findlay GM, Jones R, Procter J, Cao Y, Lamb RF. 2006. Hyperactivation of mammalian
973 target of rapamycin (mTOR) signaling by a gain-of-function mutant of the Rheb GTPase. *J*
974 *Biol Chem* **281**:19793–19797. doi:10.1074/jbc.C600028200

975 Yu CR, Power J, Barnea G, O'Donnell S, Brown HEV, Osborne J, Axel R, Gogos JA. 2004.
976 Spontaneous neural activity is required for the establishment and maintenance of the
977 olfactory sensory map. *Neuron* **42**:553–566. doi:10.1016/S0896-6273(04)00224-7

978

979

980 **FIGURE LEGENDS**

981

982 **Figure 1. The RHEBp.P37L protein is resistant to TSC complex inhibition and causes**
983 **aberrant cortical development *in vivo*.**

984 **(A)** Wild-type RHEB (WT), p.S16H or p.P37L constructs were transiently co-expressed with an
985 S6K reporter construct and the TSC complex in HEK 293T cells to assess the effect on mTORC1
986 activity. Quantification of the ratio of T389-phosphorylated S6K to total S6K was calculated
987 relative to control condition, in absence or presence of the TSC complex (control indicates empty
988 vector pcDNA3); dashed lines indicate where an irrelevant lane in the original scan was excluded
989 from the picture; bar graph represents mean \pm SEM and single data points represent the number of
990 independent biological samples per condition; for statistics see **Supplementary table 1. (B)**
991 Schematic representation of the main constructs used throughout the experiments and overview of
992 the experimental design. MCS indicate the multiple cloning site with specific restriction sites (AscI
993 and PacI in this case) to insert the gene of interest. Each construct was delivered by *in utero*
994 electroporation (IUE) at E14.5 to target the progenitor cells of layer 2/3 pyramidal neurons in the
995 somatosensory cortex (SScx); ctx=cortex; GE=ganglion eminence. **(C)** Representative confocal
996 images of the targeted SSsx counterstained with DAPI showing the transfected cells (tdTomato+)
997 in red (see also **Figure 1-figure supplement 1**) and quantification of tdTomato+ cells across the
998 different layers of the SSsx with percentage of cells reaching layer 2/3 (L2/3) in the inset (bins 1-
999 5 from the top). Dotted lines indicate the border of the intermediate zone (IZ, bottom) and delineate
1000 L2/3. Numbers in the legend indicate number of targeted mice (N=5) and total number of pictures
1001 analyzed (n=11, n=10); results are represented as mean \pm SEM and single data points in the bar

1002 graph indicate the number of pictures analyzed; inset analysis: Mann-Whitney $U = 0$, $p < 0.0001$,
1003 two-tailed Mann-Whitney test.

1004 * $p < 0.05$, ** $p < 0.01$, **** $p < 0.0001$; scale bars: 50 μm .

1005

1006 **Figure 2. Ectopic RHEBp.P37L cells display aberrant morphology and show mTOR**
1007 **hyperactivity while still preserving the molecular identity of L2/3 neurons.**

1008 **(A)** Soma size quantification of L2/3 empty vector expressing cells and RHEBp.P37L expressing
1009 cells in the nodule; box plots represent minimum and maximum values with median, dashed lines
1010 represent the mean values for empty vector (black) and for RHEBp.P37L (red); numbers indicate
1011 number of targeted mice (N=2, N=3) and number of cells analyzed (n=275, n=366); Mann-
1012 Whitney $U = 1940$, $p < 0.0001$, two-tailed Mann-Whitney test. **(B)** Reconstruction and Sholl
1013 analysis of dendritic morphology of biocytin filled cells in L2/3 of the SS_{Cx} (for empty vector
1014 control) and RHEBp.P37L cells in the nodule; numbers in the legend indicate number of targeted
1015 mice (N=3, N=2) and number of cells analyzed (n=17, n=11); data are presented as mean \pm SEM;
1016 interaction group condition/distance from the soma: $F(44, 1144) = 15.69$, mixed-effects analysis;
1017 $p < 0.0001$. **(C)** Representative images of the nodule stained with CUX1 (L2/3 marker), CTIP2 (L5
1018 marker), SATB2 (cortical projection neurons marker) or NeuN (mature neurons marker); arrows
1019 in the zoomed pictures point at examples of targeted cells; for an overview see **Figure 2-figure**
1020 **supplement 1. (D)** Representative images of the targeted L2/3 (SS_{Cx}) of empty vector control and
1021 nodule showing increased pS6-240 levels for the ipsilateral targeted cortex in RHEBp.P37L
1022 targeted mice; for an overview see **Figure 2-figure supplement 1**; bar graph represents mean \pm
1023 SEM and single data points indicate the values of each normalized ipsilateral/contralateral pS6

1024 intensity; numbers in the bars indicate number of targeted mice (N=5) and number of pictures
1025 analyzed (n=10, n=11); Mann-Whitney U = 13, $p = 0.002$, two-tailed Mann-Whitney test).
1026 Histological analysis for (A) (C) and (D) was performed on 5 weeks old mice.
1027 ** $p < 0.01$, **** $p < 0.0001$; scale bars: 20 μm (A), 50 μm (B-D).

1028

1029 **Figure 3. Overexpression of RHEBp.P37L *in vivo* causes mTORC1-dependent spontaneous**
1030 **generalized tonic-clonic seizures and abnormal neuronal network activity**

1031 (A) Timeline and experimental design indicating the cortical area targeted with the IUE and
1032 position of the electrodes placed during the EEG surgery (LSScx = left SScx; RSScx = right SScx;
1033 B = bregma; L= lambda; r = reference electrode). (B) Example EEG traces and spectrogram of 5
1034 weeks old control mouse (N=6, non-targeted mice from the same litters as the RHEBp.P37L mice)
1035 and RHEBp.P37L mouse (N=12); see also **Figure 3-figure supplement 1**; colored boxes are
1036 zoomed in panel (C). (C) Highlighted EEG traces showing: box 1. the baseline activity of a control
1037 mouse; box 2. the interictal activity, box 3. the ictal (seizure) activity and box 4. the post-ictal
1038 phase of a RHEBp.P37L targeted mouse. (D) Timeline and experimental design indicating the
1039 cortical area targeted with the IUE, the position of the electrodes for the local field potential (LFP)
1040 recordings and the IP rapamycin injections. (E) Example LFP traces for each group condition and
1041 normalized power spectrum density (PSD) averaged bilaterally over the overall consecutive days
1042 of recording (for the PSD until 50 Hz see **Figure 3-figure supplement 1**); N indicates number of
1043 mice analyzed for each group; data are represented as mean (thick line) \pm SEM (shading area). (F)
1044 Calculation of the *delta* (2-4 Hz) and *theta* (4-8 Hz) frequency bands over the total power of the
1045 PSD presented in (E), and relative ratio *theta/delta* (see also **Figure 3-figure supplement 1**); box

1046 plots represent minimum and maximum values with median, dashed lines represent the mean
1047 values for each group; for statistics see **Supplementary table 2**; * $p < 0.05$, ** $p < 0.01$, *** $p < 0.001$.

1048

1049

1050 **Figure 4. The heterotopic nodule is neither necessary nor sufficient to induce spontaneous**
1051 **seizures**

1052 **(A)** Schematic representation of the timeline of the IUE, SC rapamycin injections, EEG surgery
1053 and measurements. **(B)** Quantification of the percentage of tdTomato⁺ cells that managed to
1054 migrate out to L2/3 in mice prenatally exposed to rapamycin; data are presented as mean \pm SEM,
1055 single data points represent the values of each picture analyzed and dashed lines indicate the mean
1056 value of cells reaching L2/3 in empty vector control mice (black line) and in RHEBp.P37L mice
1057 (red line); numbers in the graph indicate number of mice (N=11, N=5) and number of pictures
1058 analyzed (n=21, n=11, n=10); (% targeted cells in L2/3: H(2) = 25.97, $p < 0.0001$, Kruskal-Wallis
1059 test; EV vs RHEBp.P37L-prenatal rapamycin, $p = 0.05$; RHEBp.P37L vs RHEBp.P37L-prenatal
1060 rapamycin, $p = 0.002$, RHEBp.P37L vs EV, $p < 0.0001$, Dunn's multiple comparisons test; *
1061 $p < 0.05$, ** $p < 0.01$. **(C)** Percentage of targeted mice showing spontaneous seizures; control mice
1062 are non-targeted mice from the same litters as the RHEBp.P37L mice prenatally exposed to
1063 rapamycin; numbers in the bar plots indicate the number of mice per group. **(D)** Representative
1064 images of RHEBp.P37L mice prenatally exposed to rapamycin that showed or did not show
1065 seizures and degree of association between the migration phenotype (mean value of % of targeted
1066 cells in L2/3, dependent scale variable, for each mouse shown in figure B) and the absence or
1067 presence of seizures (independent nominal variable) in RHEBp.P37L mice (N=4 and N=5,
1068 respectively, with the exclusion of the mice that showed heterotopia); the dashed line represents

1069 the mean value of the empty vector control group already shown in B, as comparison; $\eta_p=0.821$,
1070 $\eta_p^2=0.674$, Eta measure of association, with values of η_p close to one indicating strong association.
1071 **(E)** Schematic representation of the DNA plasmids used in the experiment. The Lox-Stop-Lox
1072 (LSL) or the floxed construct was expressed in combination with the CAGG-ERT2CreERT2 and
1073 a CAGG-DIO-EGFP constructs. The EGFP in the CAGG-DIO-EGFP construct is expressed only
1074 upon tamoxifen injection, providing a measure of efficient cre-dependent recombination. **(F)** and
1075 **(H)** Representative images showing the effect of tamoxifen administration in adult mice injected
1076 *in utero* with either the LSL construct **(F)** or the floxed construct **(G)**; mice were injected 4 times
1077 with tamoxifen starting from P7 in **(F)** and starting from P14 in **(G)** and sacrificed at P50. **(G)** and
1078 **(I)** Timeline of the experimental design and bar graphs indicating the percentage of targeted mice
1079 for each group measured with EEG until 12 weeks of age showing spontaneous seizures; numbers
1080 in the bar plots indicate the number of mice.
1081 Scale bars: 100 μm .

1082

1083 **Figure 5. RHEBp.P37L overexpression induces an increase in axon length and branching**
1084 **both *in vitro* and *in vivo***

1085 **(A)** Representative images of primary hippocampal cultures transfected at day *in vitro* 1 (DIV1)
1086 with either empty vector control or RHEBp.P37L constructs (tdTomato, in red) stained at DIV4
1087 with a pan axonal marker SMI312 (in green); arrowheads indicate the axons; bar graphs represent
1088 mean \pm SEM and single data points indicate the number of cells analyzed; numbers indicate
1089 number of neuronal cultures (N=2) and total number of cells analyzed (n=24, n=20); axonal
1090 length: Mann-Whitney U = 32, $p<0.0001$, Mann-Whitney test; axonal branches: Mann-Whitney U
1091 = 53, $p<0.0001$, Mann-Whitney test. **(B)** Overview coronal sections in grey scale stained with anti-

1092 RFP antibody of an empty vector and a RHEBp.P37L mouse brain *in utero* electroporated on the
1093 left S1 and magnification of the axon terminals on the contralateral S1; scale bars: 500 μm . (C)
1094 Representative images of ipsilateral and contralateral S1 area of an empty vector and a
1095 RHEBp.P37L mouse coronal section (P50) with quantification of the axonal projections across the
1096 different layers in the contralateral cortex measured as normalized fluorescent intensity of the
1097 tdTomato signal; numbers in the legend indicate number of targeted mice (N=3, N=4) and number
1098 of contralateral pictures (n=10, n=23) analyzed; data are presented as mean (thick line) \pm SEM
1099 (shading area); interaction group condition/cortical layers: $F(9, 279)=13.96$, $p<0.0001$, mixed-
1100 effects analysis; control vs RHEBp.P37L L2/3 (bin2-3 from the top): $p<0.0001$; control vs
1101 RHEBp.P37L L5-L6: bin7, $p=0.0074$, bin8, $p<0.0001$, bin 9, $p=0.002$; Bonferroni multiple
1102 comparisons test.
1103 ** $p<0.01$, **** $p<0.0001$; scale bars: 50 μm (A), 500 μm (B), 100 μm (C).

1104

1105 **Figure 6. Overexpressing RHEBp.P37L increases synaptic connectivity on the contralateral**
1106 **hemisphere.**

1107 (A) Schematic representation of the timeline and experimental conditions of the IUE and *ex vivo*
1108 whole-cell patch clamp recordings in contralateral L2/3 and L5 upon wide-field optogenetic
1109 stimulation. (B) Example traces and analysis of the compound postsynaptic responses after
1110 photostimulation (blue light), showing the postsynaptic response amplitudes and total charge in
1111 contralateral L2/3 and L5 in empty vector (EV) and RHEBp.P37L expressing slices; numbers in
1112 the graph indicate number of targeted mice (N=5) and number of cells (n=8, n=13, n=10, n=15)
1113 analyzed; data are presented as mean \pm SEM and single data points indicate the values of each
1114 cell; for statistics see **Supplementary table 3**; * $p<0.05$, *** $p<0.001$.

1115

1116 **Figure 7. Loss of axonal projections or blocking vesicle release of RHEBp.P37L expressing**
1117 **neurons is sufficient to stop seizures.**

1118 **(A) (C)** Schematic representation of the timeline of the IUE, EEG surgery and measurements and
1119 timepoints of tamoxifen administration in **(C)**. **(B)** Example figures of ipsilateral targeted S1,
1120 corpus callosum and contralateral S1 of an adult mouse (12 weeks) *in utero* electroporated with
1121 the RHEBp.P37L (construct expressing EGFP, in green) and a Tetanus toxin construct (TeTxLC,
1122 construct expressing tdTomato, in red). Note the absence of axonal projections on the contralateral
1123 side. The bar graph shows percentage of seizure-free targeted mice measured with EEG until 12
1124 weeks of age. Numbers in the bar graph indicate number of mice. **(D)** Example figures of ipsilateral
1125 targeted area (left) and contralateral cortex of an adult mouse (12 weeks) *in utero* electroporated
1126 with the RHEBp.P37L (in green) and a LSL-Tetanus toxin construct (LSL-TeTxLC, in red) and
1127 injected with tamoxifen starting at P14. The bar graph shows percentage of targeted mice
1128 developing seizures upon early tamoxifen injection (P14) or upon tamoxifen administration after
1129 detecting seizures and measured with EEG until 12 weeks of age (see **Supplementary table 4** for
1130 details on the timeline of the experiment). Numbers in the bar graphs indicate number of mice.
1131 Scale bars: 100 μ m.

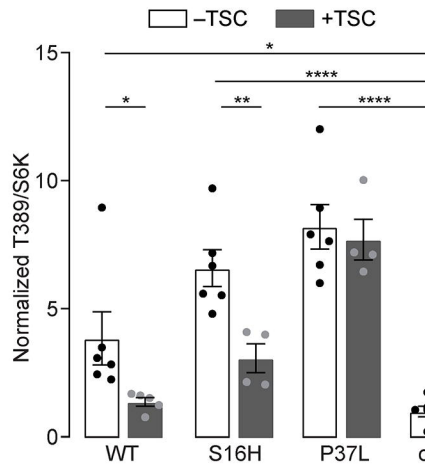
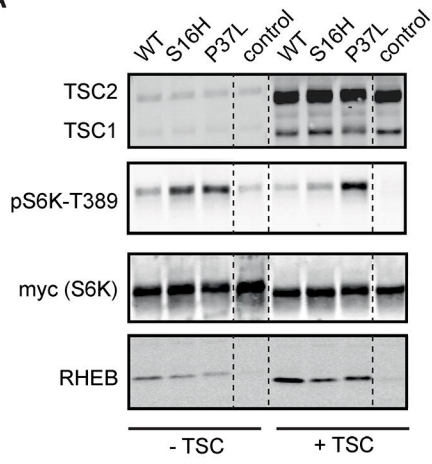
1132
1133 **Figure 8. Neurons in the contralateral homotopic cortical area in RHEBp.P37L mice show**
1134 **increased excitability that can be reversed by blocking vesicles release.**

1135 **(A)** Schematic representation of the timeline and experimental conditions of the IUE and *ex vivo*
1136 whole-cell patch clamp recordings showing the targeted cells patched in the targeted S1, L2/3 and
1137 non-targeted L2/3 cells in the ipsilateral and contralateral sides. **(B)** Analysis of the passive
1138 membrane properties (capacitance [Cm], membrane resistance [Rm] and resting membrane

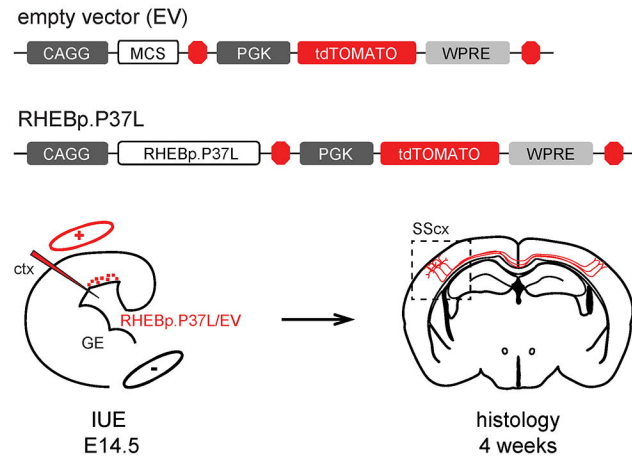
1139 potential [Vm]) of pyramidal cells in L2/3 (targeted and non-targeted) of control empty vector
1140 mice and targeted and non-targeted pyramidal cells in L2/3 of RHEBp.P37L mice; numbers in the
1141 legend indicate number of targeted mice (N=3, N=6) and number of cells (n=37, n=20, n=22,
1142 n=21) analyzed; data are presented as mean \pm SEM and single data points indicate the values of
1143 each cell; for statistics see **Supplementary table 5**). **(C)** Example traces and number of action
1144 potentials in response to increasing depolarizing currents; number of mice and cells is as indicated
1145 in **(B)**; data are presented as mean \pm SEM and the red dashed line represents the pooled mean value
1146 \pm SEM of targeted and non-targeted cells in empty vector control mice (N=3) shown separately in
1147 **Figure 8-figure supplement 1**, for comparison; for statistics see **Supplementary table 5**). **(D)**
1148 Schematic representation of the timeline and experimental conditions IUE, tamoxifen injections
1149 and *ex vivo* whole-cell patch clamp recordings in L2/3 of ipsilateral and contralateral S1 cortex.
1150 **(E)** Number of action potentials in response to increasing depolarizing currents of cells expressing
1151 both RHEBp.P37L and LSL-TeTxLC in L2/3 ipsilateral S1 and non-targeted cells in L2/3
1152 contralateral S1; data are presented as mean \pm SEM and dashed lines represent the mean values \pm
1153 SEM of the pooled control cells from empty vector mice shown in **Figure 8-figure supplement 1**
1154 and of the RHEBp.P37L mice from **Figure 8C**, for comparison; N=number of mice, n=number of
1155 cells analyzed; for statistics see **Supplementary table 6**. **(F)** Analysis of passive membrane
1156 properties (Cm, Rm and Vm) of pyramidal cells in L2/3 of mice targeted with RHEBp.P37L and
1157 LSL- TeTxLC in ipsilateral S1 and non-targeted cells on the contralateral side; data are presented
1158 as mean \pm SEM and the dashed lines indicate the mean values of capacitance, membrane resistance
1159 and resting membrane potential of RHEBp.P37L targeted cells in L2/3 and contralateral cells
1160 shown in **Figure 8B**, for comparison; for statistics see **Supplementary table 6**.
1161 * $p < 0.05$, ** $p < 0.01$, *** $p < 0.001$, **** $p < 0.0001$.

Figure 1

A



B



C

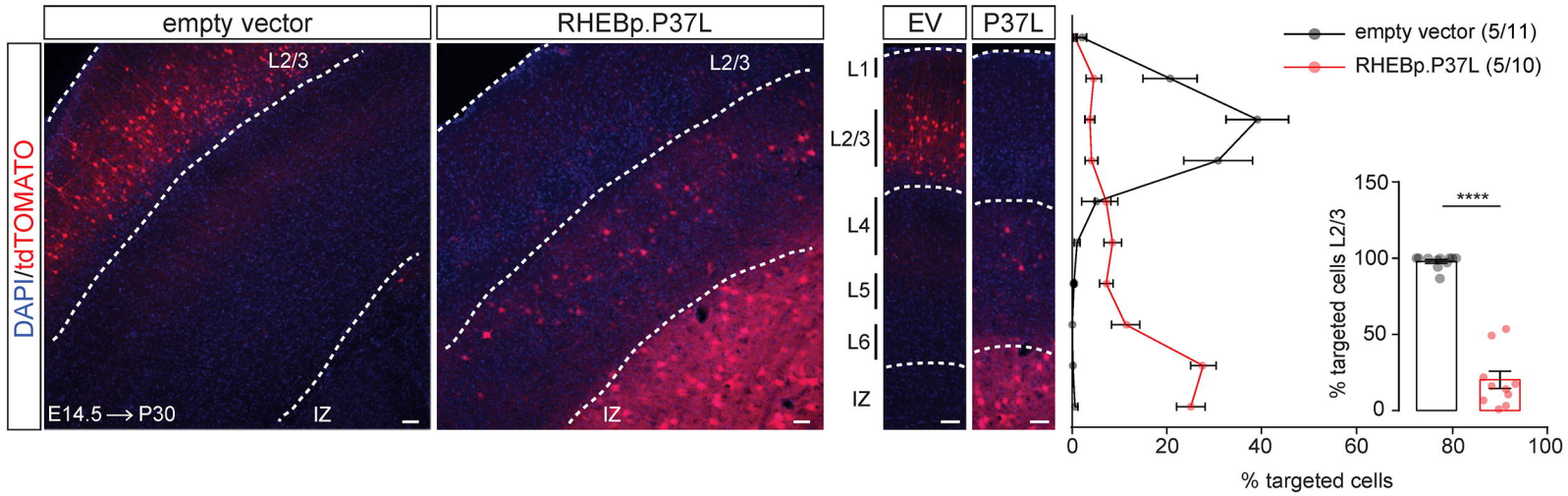


Figure 2

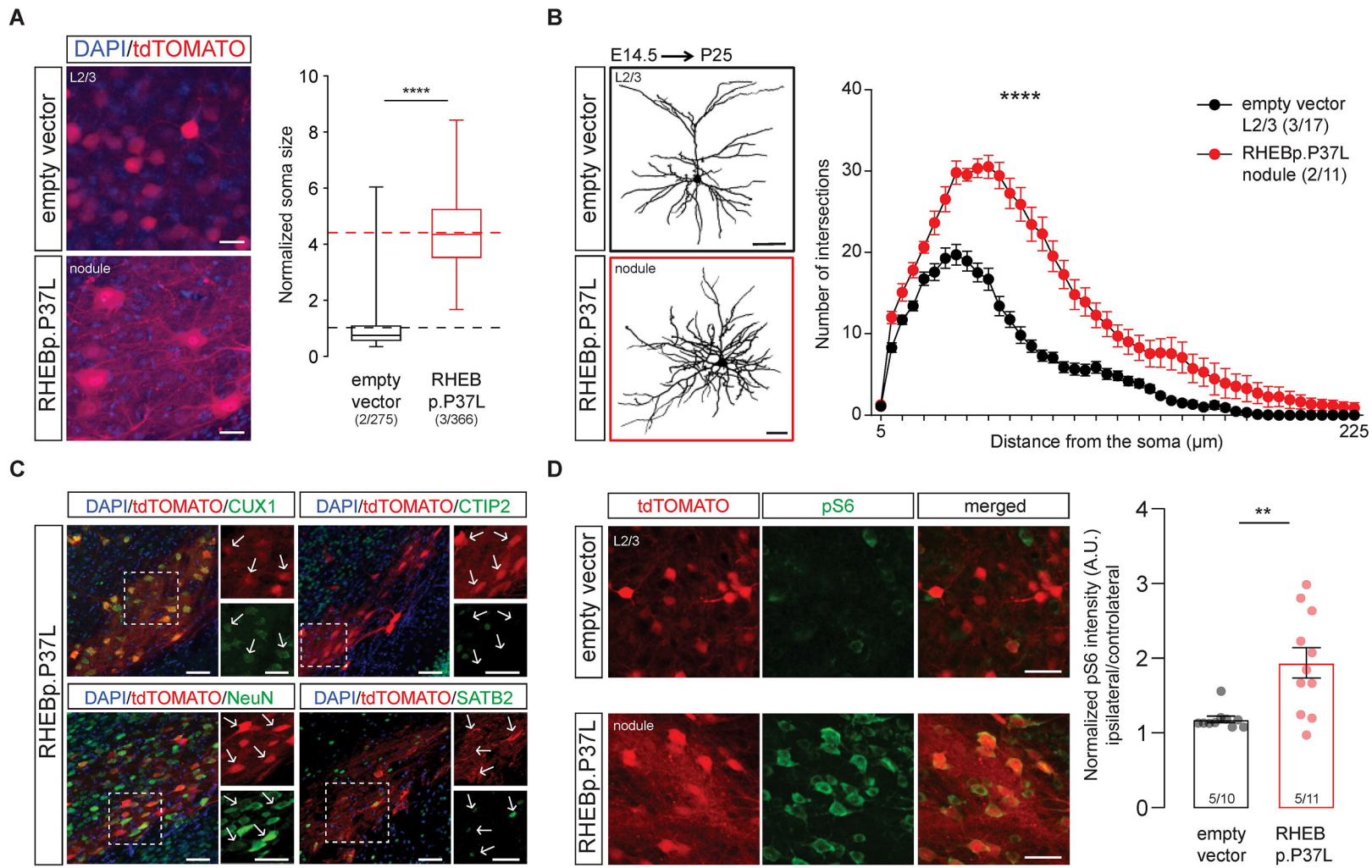
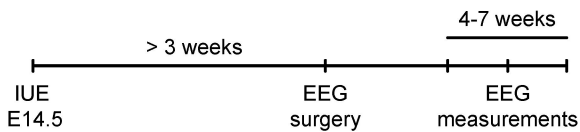
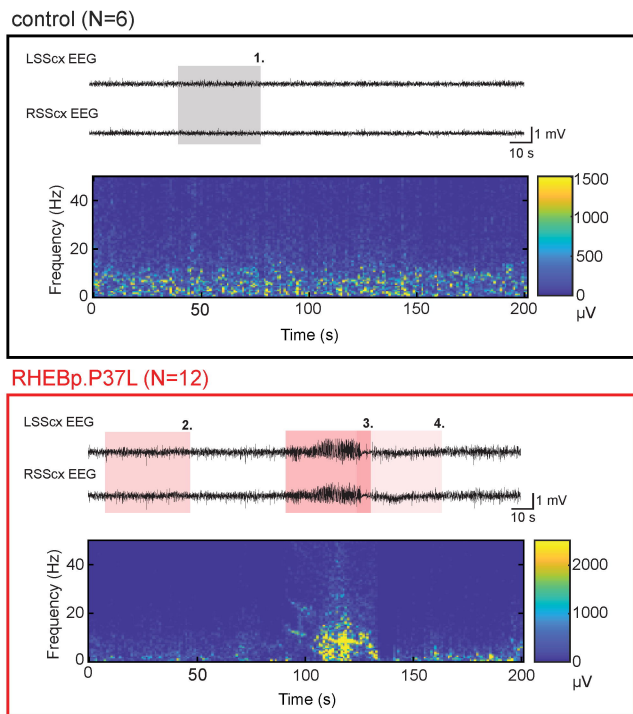


Figure 3

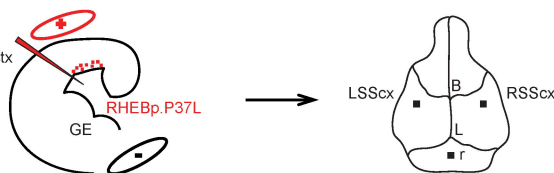
A



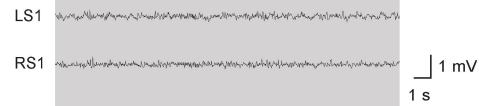
B



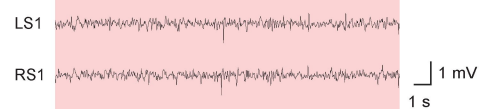
C



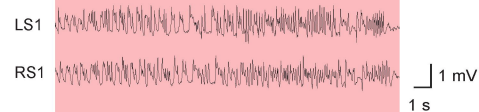
1. Baseline activity control



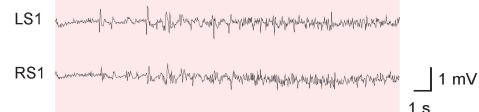
2. Interictal activity



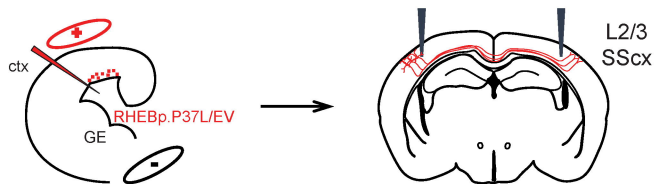
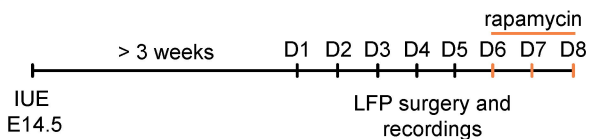
3. Ictal activity



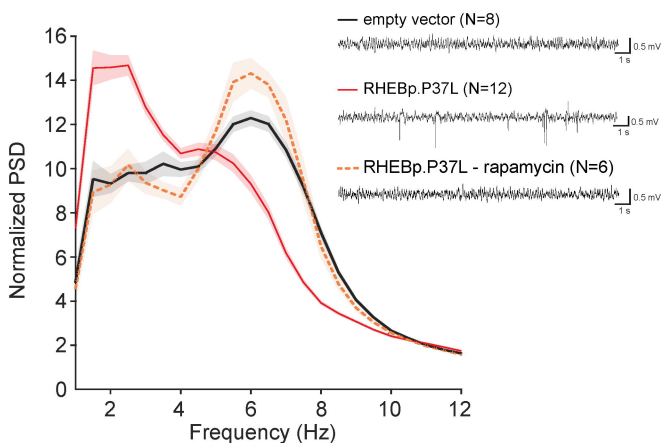
4. Post-ictal activity



D



E



F

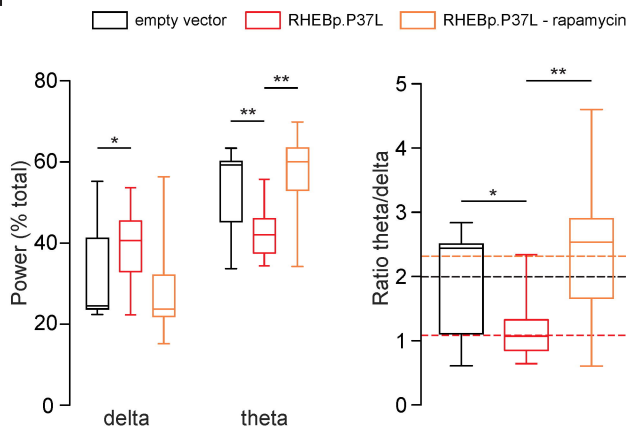


Figure 4

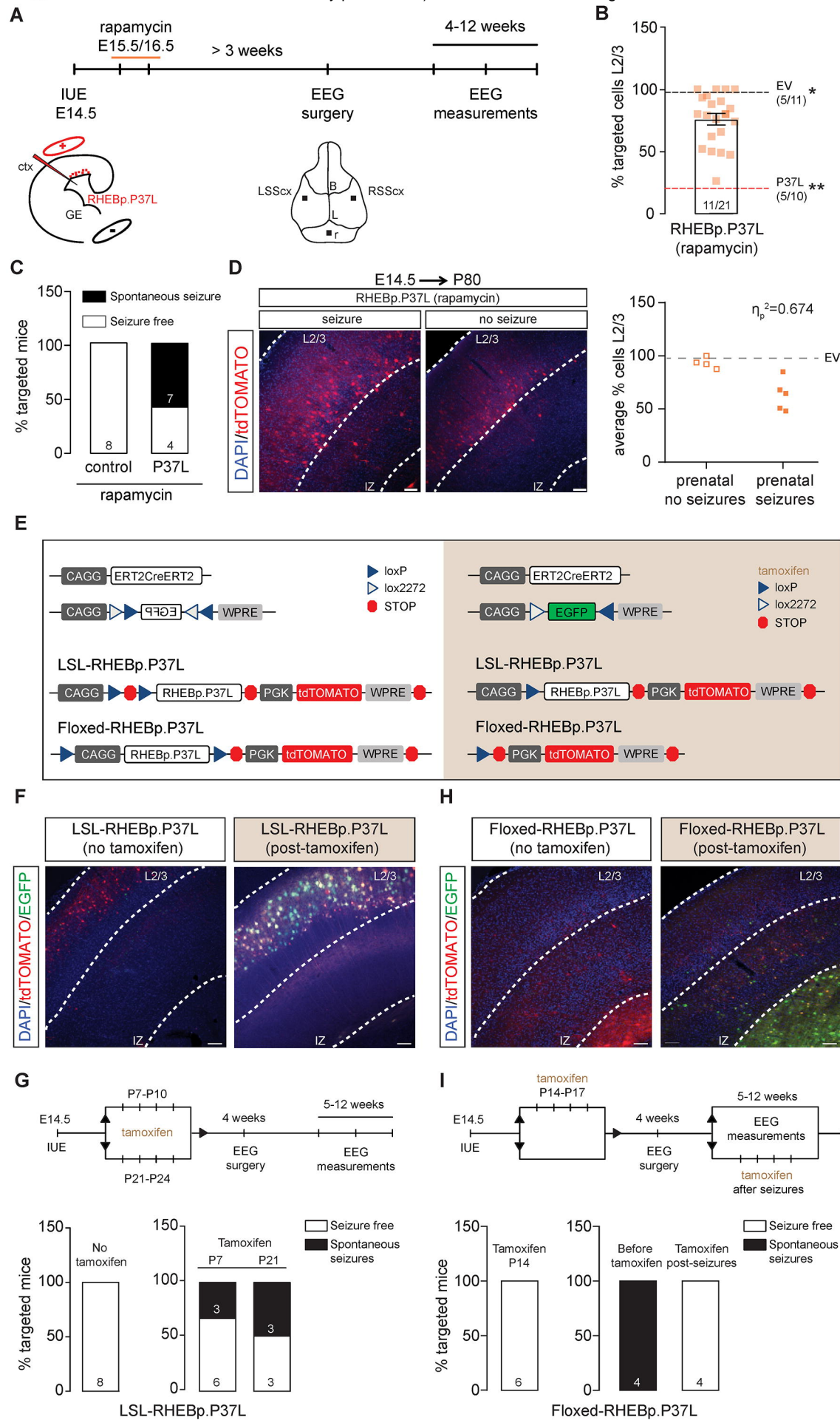
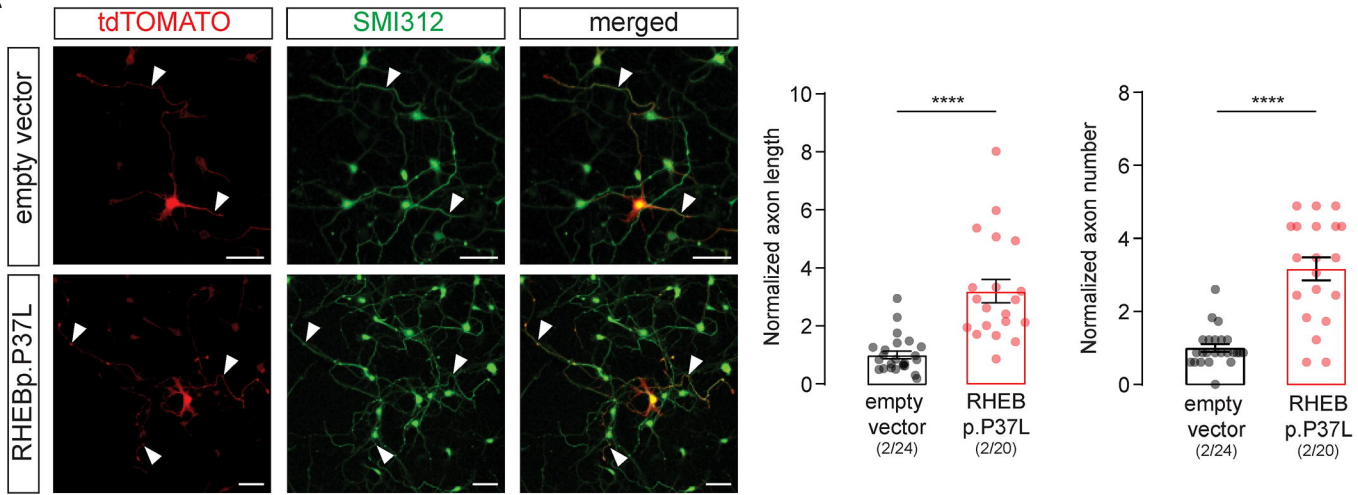
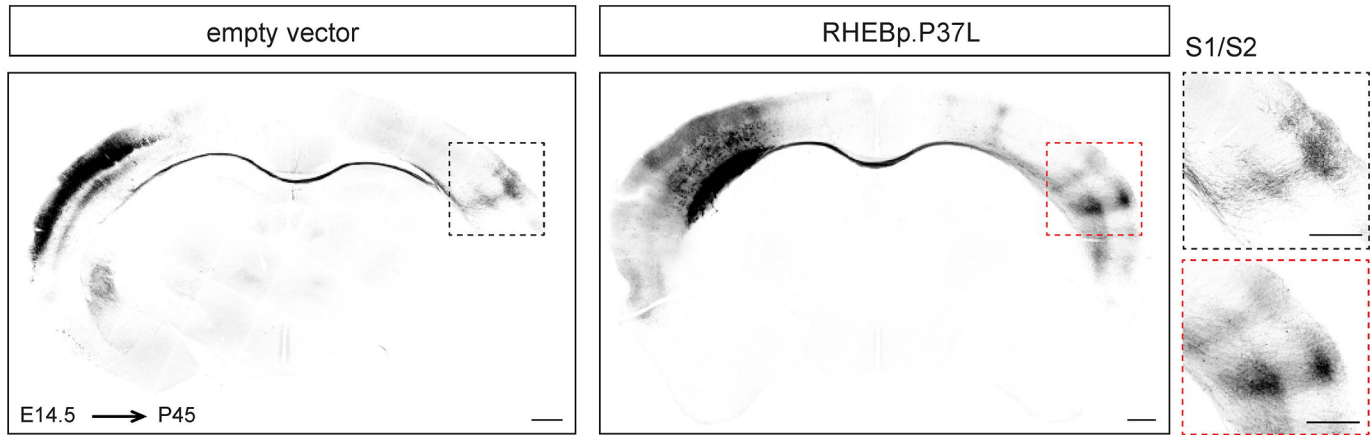


Figure 5

A



B



C

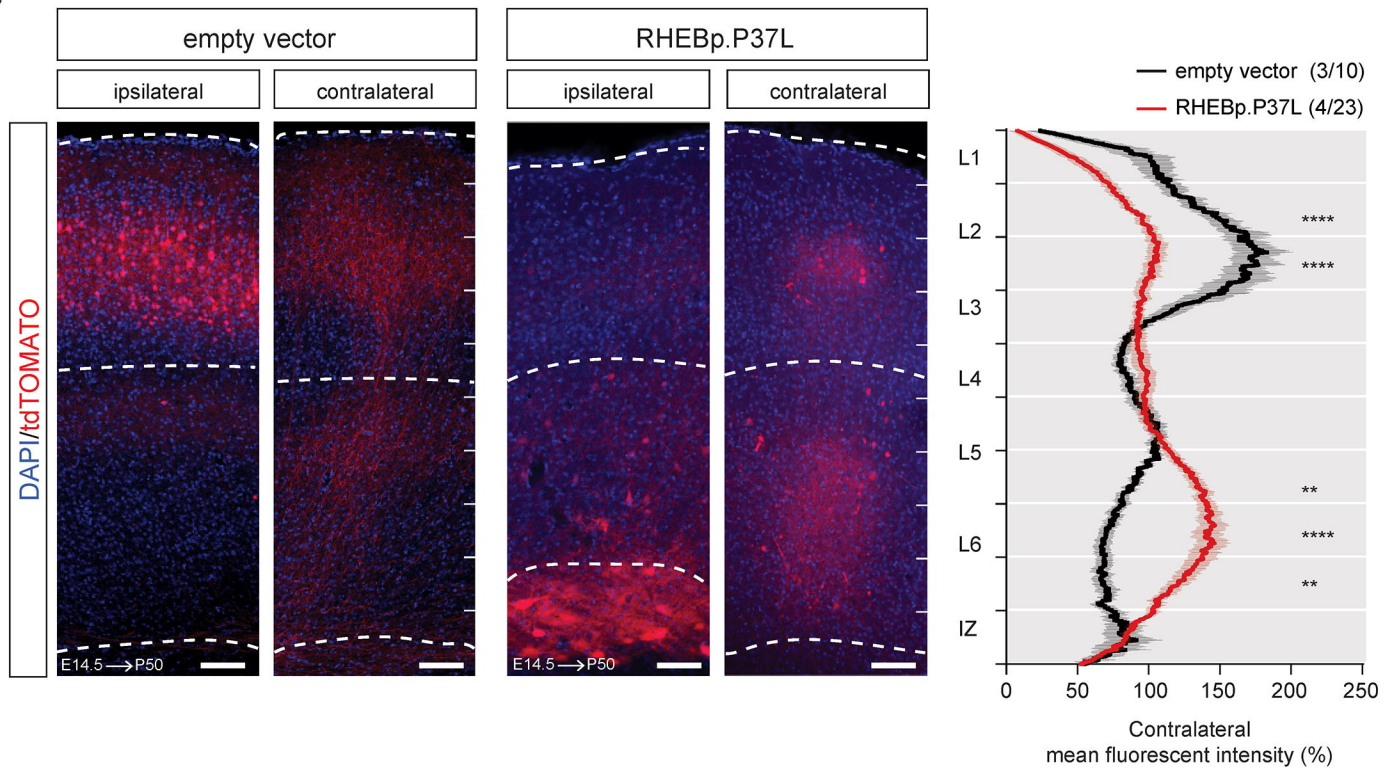


Figure 6

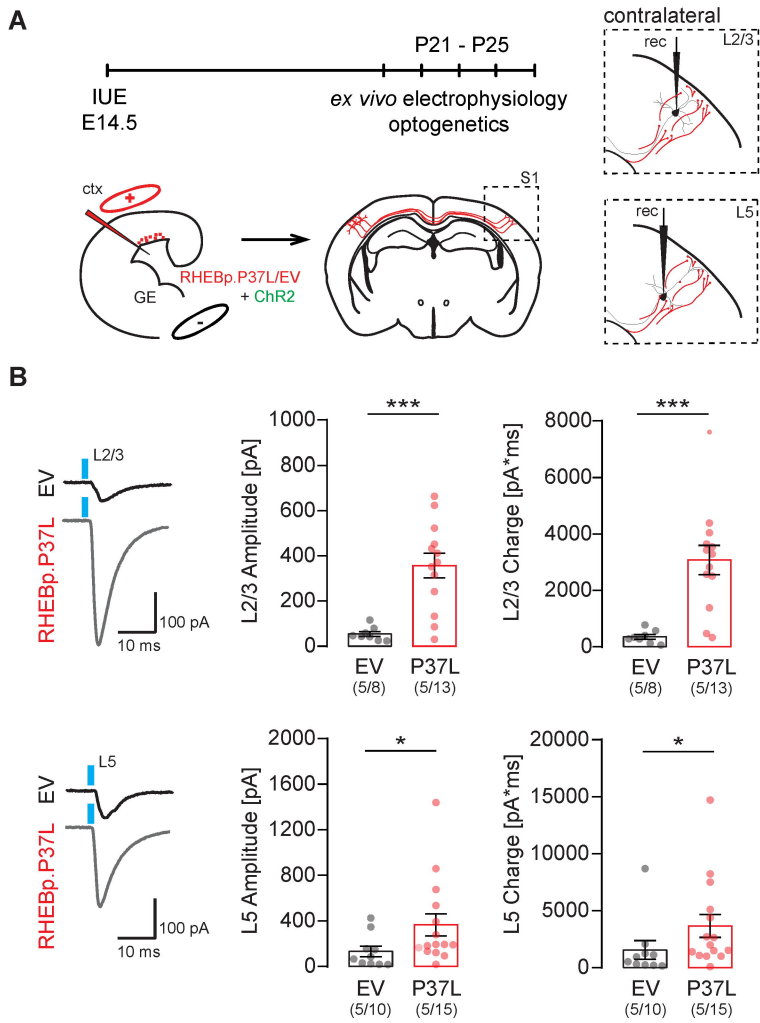


Figure 7

